# Study of the future evolution of the urban climate of Paris by statistical-dynamical downscaling of the EURO-CORDEX ensemble

Benjamin Le Roy, Aude Lemonsu, Robert Schoetter, Tiago Machado

# Study of the future evolution of the urban climate of Paris by statistical-dynamical downscaling of the EURO-CORDEX ensemble

BENJAMIN LE ROY,[a] AUDE LEMONSU,[a] ROBERT SCHOETTER,[a] TIAGO MACHADO,[a].

[a] *CNRM, Université de Toulouse, Météo-France, CNRS, Toulouse, France*

*Corresponding author*: Benjamin Le Roy, benjamin.le-roy@hereon.de

*Current affiliation*: Benjamin Le Roy's current affiliation is *Climate Service Center Germany (GERICS), Helmholtz-Zentrum Hereon, Hamburg, Germany*





**Early Online Release:** This preliminary version has been accepted for publication in *Journal of Applied Meteorology and Climatology*, may be fully cited, and has been assigned DOI 10.1175/JAMC-D-23-0145.1. The final typeset copyedited article will replace the EOR at the above DOI when it is published.

ABSTRACT

High-resolution urban climate projections are needed for local decision-making on climate change adaptation. Regional climate models have resolutions that are too coarse to simulate the urban climate at such resolutions. A novel statistical-dynamical downscaling approach (SDD) is used here to downscale the EURO-CORDEX ensemble to a resolution of 1 km while adding the effect of the city of Paris (France) on air temperature. The downscaled atmospheric fields are then used to drive the Town Energy Balance urban canopy model to produce high-resolution temperature maps over the period 1970-2099, while maintaining the city's land cover in its present state. The different steps of the SDD are evaluated for the summer season. The regional climate models simulate minimum(maximum) temperatures (TN/TX) that are too high(low). After correction and downscaling, the urban simulations inherit some of these biases, but give satisfactory results for summer urban heat islands (UHI), with average biases of -0.6 K at night and +0.3 K during the day. Changes in future summer temperatures are then studied for two greenhouse gas emission scenarios, RCP4.5 and RCP8.5. Outside the city, the simulations project average increases of 4.1 K and 4.8 K for TN and TX for RCP8.5. In the city, warming is lower, resulting in a decrease in UHIs of -0.19 K at night (from 2.1 K to 1.9 K) and -0.16 K during the day. The changes in UHIs are explained by higher rates of warming in rural temperatures due to lower summer precipitation and soil water content, and are partially offset by increased ground heat storage in the city.

## 1. Introduction

Cities alter the environment due to their 3D geometry and the materials they are made of (Arnfield 2003), which influence physical processes such as the exchange of energy, water and momentum between the surface and the atmosphere (Nunez and Oke 1977; Oke 1988). These modifications have several effects on the atmosphere near the surface, the most prominent one being the Urban Heat Island (UHI; Arnfield 2003; Rizwan et al. 2008). The urban climate (Oke et al. 2017) is associated with multiple impacts on inhabitants like health risks due to higher air temperature (Endlicher et al. 2008, Tan et al. 2010; Heaviside et al. 2016, 2017, Wong et al. 2017; Santamouris 2020) or air pollution (Leung 2015). Some of those impacts are expected to increase with ongoing global warming (Wilby 2007; Tyler and Moench 2012; Masson-Delmotte et al. 2021, Eyring et al. 2021; Seneviratne et al. 2021),





Accepted for publication in *Journal of Applied Meteorology and Climatology*. DOI 10.1175/JAMC-D-23-0145.1.

especially heat stress because of higher temperature (McMichael et al. 2006; Buzan et al. 2020) and more frequent and severe extreme events (Luber and McGeehin 2008; Domeisen et al. 2023).

The Global Climate Models (GCM) and Earth System Models (ESM) that are used to project the future warming at the global (Lee et al. 2021) and regional (Doblas-Reyes et al. 2021) scales are not adapted to urban-scale impact studies because of their too coarse resolution (between tens to hundreds of kilometers). Different avenues exist to bridge the gap between the global and local scales (Wilby and Wigley 1987; Ekström et al. 2015; Xu et al. 2019). Dynamical downscaling (Giorgi and Gutowski 2015; Xu et al. 2019; Tapiador et al 2020; Lucas-Picher 2021) consists of coupling GCMs to limited-area Regional Climate Models (RCM, Rummukainen 2010, 2016) that now reach the kilometer scale and can represent cities (Trusilova et al. 2013; Hamdi et al 2014, 2015; Lauwaet 2015a, 2015b; Zhao et al. 2018; Daniel et al. 2019; Sharma et al. 2019; Lo et al. 2020; Keppas et al. 2021; Keat et al. 2021; Lind et al. 2022; Lemonsu et al. 2023) when coupled to Urban Canopy Models (UCM; Oke 1984; Masson 2006; Grimmond et al. 2010). Dynamical downscaling makes it possible to simulate local physical processes (Rummukainen 2010, 2016) and allows to represent the feedback between the urban and the regional climate (Daniel et al. 2019) but it comes at a great computational cost and is often limited in time (some decades for a few scenarios of greenhouse gas emissions). Statistical downscaling is another methodology (Giorgi et al. 2001; Wilby et al 2004; Schoof 2013; Doblas-Reyes et al. 2021), which relies on the establishment of statistical relationships between the global and the local scales over a period in the past and applies these relationships in the future where the global scale is simulated but the local scale is missing. Statistical downscaling is computationally cheap compared to dynamical downscaling but it is associated with uncertainties (Dixon et al. 2016; Salvi et al. 2016) since it relies on the availability of local scale observations of the past, which can be challenging for urban environments (Stewart, 2011; Chen et al. 2012), and also on the hypothesis that the relationships found in the past climate will hold true in the future climate.

In this study, a combination of both approaches – that is referred as statistical-dynamical downscaling (SDD; Frey-Buness et al. 1995; Mengelkamp et al. 1997; Fuentes 2000; Boé et al. 2006; Früh et al. 2011; Žuvela-Aloise et al. 2016; Hoffmann et al. 2018; Schoetter et al.





Accepted for publication in *Journal of Applied Meteorology and Climatology*. DOI 10.1175/JAMC-D-23-0145.1.

2020; Duchêne et al. 2020, 2022; Le Roy et al. 2021) – is used to add the local effect of the city on the air temperature to temperature fields simulated by regional climate projections not taking into account urban land surfaces (Langendijk et al. 2019; Le Roy et al. 2021). The approach builds on previous work (Hoffmann et al; 2018; Schoetter et al. 2020; Le Roy et al. 2021) and was already presented and evaluated for near surface UHIs by Le Roy et al. (2021). It is extended here to create above-canopy air temperature fields at the sub-daily time steps that are then used to drive a land surface model (LSM) coupled to a UCM at high-resolution over the city of Paris, France. The different steps of the downscaling and the data used are presented in section 2. The resulting urban climate simulations are first evaluated against observations (section 3) and then used to study the evolution of future daily minimum (TN) and maximum air temperature (TX) and associated UHIs (section 4). Previous studies that have investigated the evolution of UHIs under climate change have found that when future urbanization is not represented, the UHI intensity change is projected to be an order of magnitude smaller than the background warming signal (Doblas-Reyes et al. 2021, box 10.3). They also noted conflicting results regarding the sign of the change depending on the cities studied and the approaches used. Here, different physical mechanisms are analyzed to better understand the projected evolution of Paris thermal urban climate (section 5).

## 2. A downscaling framework for urban climate impact studies

Long-term simulations of the local and urban climate of Paris region (France) are carried out with a kilometric horizontal resolution and a UCM. This section describes the regional climate projections used, which are based on multiple couples of GCMs/RCMs, the spatial downscaling method implemented to combine the RCM results with the influence of the city on the local climate, and the LSM employed to simulate the surface energy balance.

### *a. Regional climate change projections*

The climate projections on which the spatial downscaling is applied come from the ensemble of regional climate simulations EURO-CORDEX (Jacob et al. 2014, Jacob et al. 2020, see domain in Fig. 1.a). All the selected RCMs have a resolution of 0.11° (about 12.5 km; Fig. 1.b) and are driven by CMIP5 GCMs and ESMs (Taylor et al. 2012). Two Representative Concentration Pathway scenarios (RCP; Van Vuuren et al. 2011) are used.





Accepted for publication in *Journal of Applied Meteorology and Climatology*. DOI 10.1175/JAMC-D-23-0145.1.

These are the highest emissions scenario with continuously increasing emissions RCP8.5 (Riahi et al. 2011) and the more moderate RCP4.5 where emissions from fossil fuels use start to decline around 2040 (Thomson et al. 2011). The choice of scenarios was made to obtain the greatest number of simulations available with the necessary sub-daily RCM outputs required to drive the urban climate simulations. In total, 41 couples of GCM/RCM are used for the historical period and the RCP8.5 scenario, and 14 couples for the RCP4.5 scenario (Fig. 2). GCM/RCM couples that are available for RCP4.5 but not for RCP8.5 are excluded. Each GCM is represented a similar amount of times in the two ensembles (around 2 (7) times in RCP4.5 (8.5), with the exception of the GCMs IPSL-CM5A-MR (1 (4)) and MPI-ESM-LR (1 (8)). The ensemble of 41 simulations is used for the evaluation of the downscaling in the historical climate and the ensemble of 14 simulations for the future climate. When justified, comparisons between the 14 and 41 ensembles statistics are detailed in the text. Uncertainties are not directly estimated but instead the model spread is displayed as the interquartile range of the ensemble computed using quantile estimates following the algorithm of Hyndman and Fan (1996), which is implemented in R as default type 7 (R Core Team, 2022).





Accepted for publication in *Journal of Applied Meteorology and Climatology*. DOI 10.1175/JAMC-D-23-0145.1.

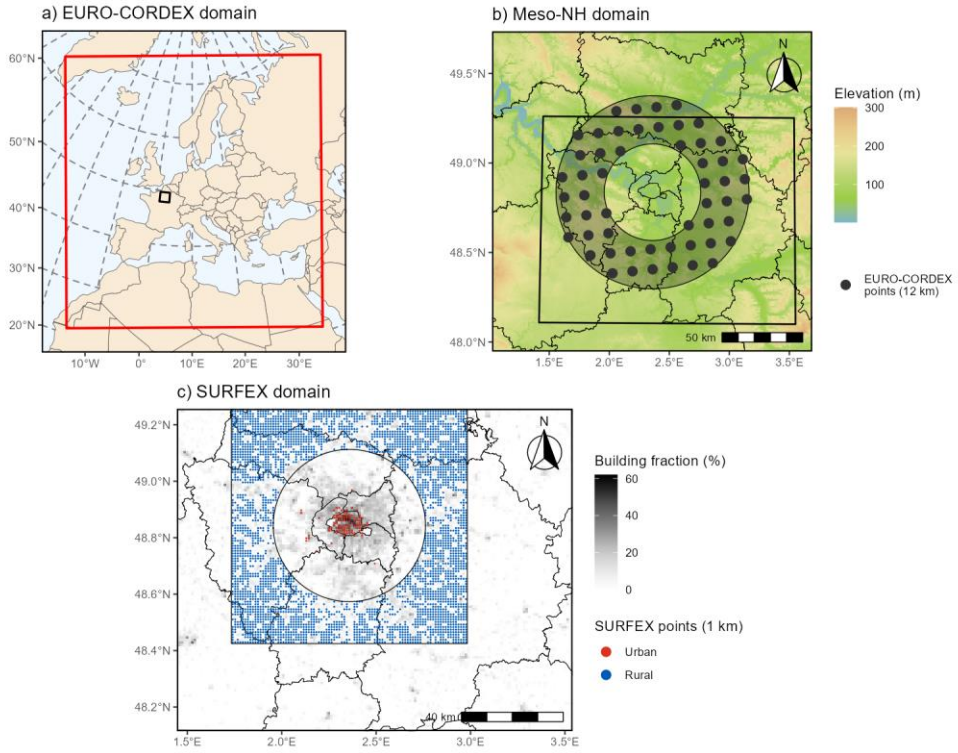


Fig. 1. Simulation domains. a) EURO-CORDEX domain (red) and Meso-NH domain (black) used for the SDD. b) Meso-NH domain, SURFEX domain (black rectangle) and ring used to extract rural CORDEX points. c) SURFEX domain with the building fraction and the points defined as urban and rural for the analysis.





Accepted for publication in *Journal of Applied Meteorology and Climatology*. DOI 10.1175/JAMC-D-23-0145.1.

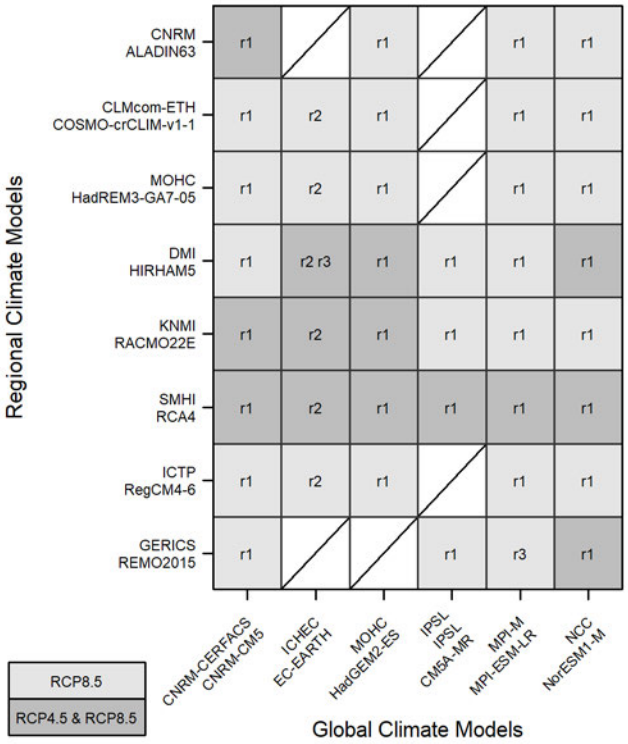


Fig. 2. Matrix of all the CMIP5/EURO-CORDEX GCM/RCM couples used in the present study under the greenhouse gas emissions scenarios RCP4.5 (14 in dark gray) and RCP8.5 (41 in light and dark gray). “r1”, “r2” and “r3” represent the ensemble member used for each simulation (r1i1p1, r2i1p1 and r3i1p1). References of each GCM and RCM can be found in Table S1 and Table S2 in the online supplemental material.

The use of a subset of simulations instead of the full “ensemble of opportunity” can have an impact on the projected degree of warming (Mezghani et al, 2019). Here, the smaller ensemble of 14 simulations is quite close to the full ensemble with a slight overestimation of warming over the whole year (ANN, not exceeding 0.2 K) and in winter (DJF) for TN and TX, in summer (JJA) for TN, and an underestimation of TX in JJA (Fig. S1 in the online supplemental material).

The spatial downscaling method is applied to the ensemble of climate projections. To prevent the possible double counting of urban effects when RCMs describe urban areas as rocky covers (Langendijk et al. 2019), all the RCM variables used are extracted and averaged from points located in a ring between 30 and 60 km away from Paris center (Fig. 1.b). This simple approach is possible for the Paris region, because there are only small height differences, no large water bodies, and a relatively homogeneous land use. To apply the





Accepted for publication in *Journal of Applied Meteorology and Climatology*. DOI 10.1175/JAMC-D-23-0145.1.

downscaling framework to cities located in more geographically complex regions, the selection of points representing the rural environment might have to be refined based on the difference in altitude with the city center, the presence of water bodies, or other geographical features. As this area does not have a large difference in altitude with Paris or large bodies of water (at this resolution), it is considered sufficiently representative of the Paris climate. In addition, to produce impacts indicators associated with temperature thresholds, the RCM variables need to be corrected. Here the choice is made to only correct the RCM temperature outputs, using monthly averages of daily average temperature (TM=(TN+TX)/2) from the spatialized observation dataset AURELHY (Canellas et al. 2014) over the period 1976–2005 (see section A in the online supplemental material for more details).

*b. A statistical-dynamical downscaling for the Urban Heat Island*

The SDD approach builds on previous work devoted to the downscaling of UHI in climate projections (Hoffmann et al 2018, Schoetter et al. 2020; Duchêne et al. 2020). The different steps are highlighted in Figure 3 and the approach was first described in Le Roy et al. (2021) who used it to produce and evaluate 1 km resolution maps of UHI at 2 m above ground level covering the Paris region and the time period 2000–2009.





Accepted for publication in *Journal of Applied Meteorology and Climatology*. DOI 10.1175/JAMC-D-23-0145.1.

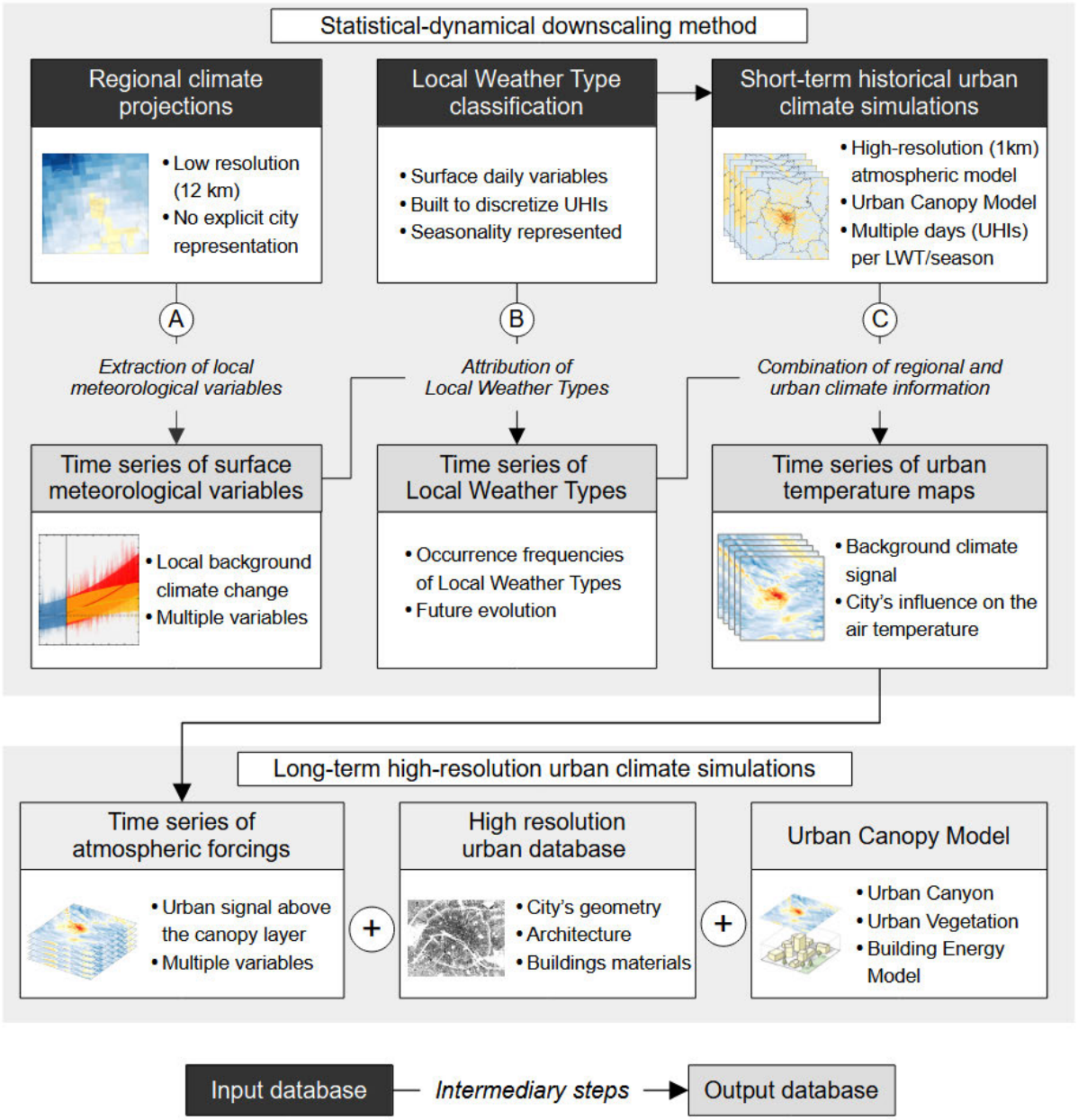


Fig. 3. Flow chart of the approach used to downscale regional climate projections to the city level.

The SDD makes use of two databases. The first one is a reference climatology of Local Weather Types (LWT) produced by Jougla et al. (2019) for several French cities, following a clustering approach developed by Hidalgo et al. (2014) and Hidalgo and Jougla (2018). The clustering model regroups different days in multiple classes with similar local weather conditions based on the daily temperature amplitude, the daily accumulated precipitation, and the daily averages of specific humidity, wind speed, and wind direction. Based on these LWT climatologies, Schoetter et al. (2020) simulated the urban climate of several of the most





Accepted for publication in *Journal of Applied Meteorology and Climatology*. DOI 10.1175/JAMC-D-23-0145.1.

representative days for each LWT using the mesoscale atmospheric model Meso-NH (Lafore et al. 1998; Lac et al. 2018) coupled to the same land surface modeling system as detailed in section. 2.3.

Schoetter et al. (2020) used both databases to reconstruct daily maps of the UHI for Toulouse and Dijon (France) by linking day-to-day information on current LWT and simulated UHI per LWT. By applying the method to reanalysis-driven RCMs for Paris, Le Roy et al. (2021) have shown that it is able to reconstruct the past climatologies of nighttime UHIs with a bias of 0.1 K in JJA. Here it is applied in a similar fashion to downscale, and correct with the UHI effect, the temperatures of EURO-CORDEX regional climate projections for the time period 1970–2099 in the strongly urbanized Paris region. Compared to the SDD introduced by Le Roy et al. (2021), here the 3-hourly variables are downscaled, and instead of near surface, above canopy (50 m) UHI fields are produced following the iterative method of Lemonsu et al. (2013). More details regarding the configuration of the Meso-NH model are given by Schoetter et al. (2020) and Le Roy et al. (2021). See section B in the online supplemental material for more details on the sub-daily downscaling approach.

*c. Land Surface Modeling*

To simulate the evolution of the urban climate of Paris, we use the LSM SURFEX (Masson et al. 2013), which incorporates the latest version of the TEB model (Masson 2000, Redon et al. 2020) to represent cities, and the ISBA model (Noilhan & Planton, 1989; Noilhan & Mahfouf, 1996) for natural areas. TEB is a state-of-the-art UCM that represents the city as a representative infinitely-long street canyon and computes separate energy budgets for each surface of the canyon (i.e. roof, wall, and road). Numerous features have been added to TEB since its initial version. These are: multiple atmospheric levels inside the canopy layer (Hamdi and Masson, 2008), urban ground vegetation and trees (Lemonsu et al. 2012, Lemonsu et al. 2021, Redon et al. 2017, Redon et al. 2020), Building Energy Model (BEM, Bueno et al. 2012, Pigeon et al. 2014) with detailed behaviors of inhabitants regarding energy usage (Schoetter et al. 2017), and the computation of outdoor thermal comfort indices (Kwok et al. 2019, Redon et al. 2020).





Accepted for publication in *Journal of Applied Meteorology and Climatology*. DOI 10.1175/JAMC-D-23-0145.1.

For the present study, the simulation domain (Fig. 1.c) covers the French administrative region Île-de-France at 1 km horizontal resolution (157 km × 128 km). SURFEX needs detailed information of the land cover and associated physical parameters, e.g. leaf area index for the vegetation or building height in the city. The default database used by SURFEX is ECOCLIMAP (Champeaux et al. 2005; Faroux et al. 2013). It contains a 1 km resolution map of land cover and associated land surface parameters. It is here combined with the MApUCE urban indicators database (Bocher et al. 2018) to refine the city description, i.e. the morphology parameters as well as the type and use of buildings. Updated urban vegetation maps separating low vegetation and tree strata have been produced by Bernard et al. (2022) using a database of the Paris region urban planning agency. Except for the refinement of low and tree vegetation, the urban database is the same as that of the Meso-NH simulations that are used to produce the atmospheric forcings (section 2.2; Schoetter et al. 2020).

SURFEX is employed in a stand-alone configuration, i.e. driven by prescribed atmospheric conditions. These include downwelling direct and diffuse solar and terrestrial radiation, atmospheric pressure, liquid and solid precipitation rate, air temperature, specific humidity, and wind speed. SURFEX is driven by the climate projection results (section 2.1) from 1970 to 2099 at a three-hourly time frequency; the first two years are used as spin-up and not analyzed. Since the direct and diffuse components of the solar radiation are not always available, they are computed from the total solar radiation using Erbs et al. (1982) formulation. Similarly, total precipitation rate is divided into liquid and solid using a 1 K threshold following Jennings et al. (2018) (see section B in the online supplemental material for more details).

The land cover does not evolve during the simulation, which allows to study the effect of a changing climate on a static (present-day) city. In future studies, the same downscaling framework could be applied to an evolving city (Lemonsu et al. 2015, Lemonsu et al. 2021) based on socioeconomic scenarios (Viguié et al. 2014; Aguejdad et al. 2016) to analyze the combined effects of urbanization and climate change (Chapman et al. 2017).





Accepted for publication in *Journal of Applied Meteorology and Climatology*. DOI 10.1175/JAMC-D-23-0145.1.

## 3. Evaluation of the historical climate simulations

The simulations are made in transient mode from 1970 to 2099; three time periods are analyzed. These are the historical period 1976–2005, the near future 2030–2049, and the far future 2080–2099. The historical period is the same as the one used to correct the ensemble average temperature, but twenty-year periods are chosen for the future to better capture the effect of climate change at the end of the century under RCP8.5 (Scherrer et al. 2006; Krakauer and Devineni, 2015; Rigal et al. 2019). Over the historical period, the annual average TM of the ensemble (41 simulations) is 12.9 °C [12.8 °C – 13.1 °C] over the city and 11.1 °C [11.0 °C – 11.1 °C] in the countryside. The temperature ranges from 6.6 °C [6.2 °C – 6.8 °C] in winter (DJF) to 19.7 °C [19.5 °C – 19.8 °C] in JJA inside Paris, and 4.3 °C [4.3 °C – 4.4 °C] to 18.2 °C [18.2 °C – 18.3 °C] in the surrounding rural areas.

*a. Observation-based data*

The urban climate simulations are evaluated for the historical period by comparison with local observations of radiation, precipitation, and temperature (Table 1). The variables are evaluated over different time periods depending on their availability; the RCP8.5 simulations are used for the years after 2005. The downwelling total shortwave (SW) and long-wave (LW) radiation are measured at the IPSL's atmospheric observatory SIRTA between 2003 and 2017 (Haeffelin et al. 2005). The daily amount of precipitation is retrieved from the COMEPHORE re-analaysis of hourly precipitation at 1 km resolution over the 2000-2017 period (Tabary et al. 2012). The temperature observations come from the 1.25 km resolution gridded dataset developed specifically for the IDF region by Kounkou-Arnaud & Brion between 2000 and 2017 (2018; KAB18) to spatialize TN and TX recorded by the Météo-France weather stations by accounting for the urbanization effects on temperature. This product has been presented and used in a previous study of Paris UHI climatology (Le Roy et al. 2021) and for model evaluation (Lemonsu et al. 2023). Over non-urbanized areas, it is comparable to the product AURELHY, which was used for the RCM correction in section 2.2. In order to be comparable with observations, SURFEX calculates TN and TX daily from the lowest and highest temperatures at each model time step (5 minutes). The nighttime UHI ($UHI_N$) is calculated with a daily time step as the difference between the minimum daily temperature averaged over urban grid points ($TN_{URB}$) and the minimum daily temperature





Accepted for publication in *Journal of Applied Meteorology and Climatology*. DOI 10.1175/JAMC-D-23-0145.1.

averaged over non-urban grid points ($TN_{RUR}$). The daytime UHI ($UHI_X$) is calculated in the same way based on daily maximum temperature (TX). The urban and rural masks shown in Fig. 1.c are computed using the MApUCE urban database. All the points in a radius smaller than 30 km defined as “Continuous buildings with enclosed island” or “Tall buildings” are considered urban while all the points outside a radius of 30 km and for which no information regarding building type is available – and consequently where the TEB model is not run – are considered rural.

For both the incident radiation components and the precipitation, the biases are exclusively inherent to the EURO-CORDEX members used to build the climate forcings of the SURFEX simulations. For surface air temperature, the differences in the simulations result from the combination of biases in the RCMs, UHI biases introduced into the forcings by the SDD method, and biases inherent to the SURFEX model itself.





Accepted for publication in *Journal of Applied Meteorology and Climatology*. DOI 10.1175/JAMC-D-23-0145.1.

| | Observation<br><br>Average (Sd) | Simulation (14)<br><br>Average (Sd) | Simulation (41)<br><br>Average (Sd) | Bias (14)<br><br>Average | Bias (41)<br><br>Average |
|---|---|---|---|---|---|
| SW ($W.m^{-2}$) | 224 (74) | 228 (22) | 234 (23) | +4.0 (+1.6%) | +9.9 (+4.4%) |
| LW($W.m^{-2}$) | 353 (21) | 353 (22) | 350 (23) | +0.4 (+0.1%) | -2.8 (-0.8%) |
| RR ($mm.d^{-1}$) | 2 | 2.4 | 2.2 | +0.4 (+18%) | +0.1 (+7%) |
| $TN_{URB}$ (°C) | 15.4 (2.9) | 16.3 (2.6) | 16.4 (2.8) | +0.8 | +1.0 |
| $TN_{RUR}$ (°C) | 12.7 (3.0) | 14.2 (2.8) | 14.2 (2.9) | +1.5 | +1.6 |
| $TX_{URB}$ (°C) | 24.8 (4.4) | 24.1 (4.1) | 24.0 (4.2) | -0.7 | -0.8 |
| $TX_{RUR}$ (°C) | 24.4 (4.3) | 23.2 (4.2) | 23.3 (4.3) | -1.2 | -1.1 |
| $TM_{URB}$ (°C) | 20.1 (3.3) | 20.2 (3.2) | 20.2 (3.3) | 0.0 | +0.1 |
| $TM_{RUR}$ (°C) | 18.5 (3.1) | 18.7 (3.3) | 18.7 (3.4) | +0.2 | +0.2 |
| $UHI_N$ (°C) | 2.8 (1.4) | 2.1 (0.7) | 2.2 (0.8) | -0.7 | -0.6 |
| $UHI_X$ (°C) | 0.5 (0.6) | 0.9 (0.5) | 0.8 (0.5) | +0.4 | +0.3 |
| $P_{90}UHI_N$ (°C) | 4.6 | 3.0 | 3.2 | -1.6 | -1.4 |
| $P_{90}UHI_X$ (°C) | 1.2 | 1.5 | 1.4 | +0.3 | +0.3 |

Table 1. Summer (JJA) average and standard deviation of different observation datasets, of the 14 simulations ensemble and average biases. Observation datasets used: temperature KAB18 (2000–2017); shortwave (SW) and long-wave (LW) radiation – SIRTA (2003–2017); precipitation (RR) – COMEPHORE (2000–2017). Simulation refers to SURFEX simulations for the temperatures and RCM outputs for SW, LW and RR. The simulation values are computed using the historical experiment before 2005 and the RCP8.5 afterwards. The standard deviation of the simulations represents the square root of the average of each simulation variance rather than the ensemble average of each simulation standard deviation.





Accepted for publication in *Journal of Applied Meteorology and Climatology*. DOI 10.1175/JAMC-D-23-0145.1.

*b. Downwelling radiation and precipitation*

The EURO-CORDEX models capture well both shortwave and long-wave incoming radiation between 2003 and 2017. Average daytime SW is overestimated by 9.9 $W.m^{-2}$ (4.4%) [-10.7 $W.m^{-2}$ – 25.1 $W.m^{-2}$]; with the overestimation being mostly due to the direct component. Average LW is underestimated by 2.8 $W.m^{-2}$ (0.8%) [-8.5 $W.m^{-2}$ – 2.3 $W.m^{-2}$]. As noted by previous studies, the EURO-CORDEX RCMs simulate too much precipitation both when driven by reanalysis data (Kotlarski et al. 2014; Prein et al. 2016) and by GCMs (Vautard et al. 2021). This is confirmed here with 0.1 mm too much rain per summer day (7%) between 2000 and 2017, and with a clear influence of the driving GCM. For example CNRM-CM5 simulates the highest precipitation amount (GCM average of 2.7 $mm.d^{-1}$ vs. the ensemble [41] average of 2.2 $mm.d^{-1}$) and HadGEM2-ES the lowest (GCM average of 1.7 $mm.d^{-1}$).

*c. Temperature and Urban Heat Island*

TN and TX of the RCMs are corrected before running the SURFEX simulations by the monthly TM bias, using the AURELHY data for 1976–2005 as a reference. Before the bias correction, the full ensemble (41) simulates too high $TN_{JJA}$ with 0.7 K [-0.3 K – 1.4 K] (Table S4 in the online supplemental material) and too low $TX_{JJA}$ with -1.3 K [-2.6 K – -0.3 K] ($TM_{JJ}A$ bias: -0.3 K [-1.4 K – 0.5 K]), which was already found by Vautard et al. (2021). The small ensemble average bias in $TN_{JJA}$ results from a compensation of negative biases in RACMO22E and RCA4 and positive biases in the other simulations, notably the one driven by HadGEM2-ES. After the TM correction, the ensemble biases are 1 K [0.7 K – 1.3 K] and -1 K [-1.3 K – -0.6 K] for $TN_{JJA}$ and $TX_{JJA}$, respectively; the simulated daily temperature amplitude is therefore too low.

Compared to the KAB18 dataset over the period 2000-2017, the simulations have positive biases in $TN_{JJA}$ over both urban and rural areas, but of different magnitudes (0.8 K and 1.5 K, respectively). Given that $TM_{RCM}$ was corrected, the final biases in $TM_{URB}$ and $TM_{RUR}$ are necessarily introduced by the SDD and the SURFEX simulations. It is found that the SDD and SURFEX do not add significant TM biases (+0.1 K and +0.2 K for $TM_{URB}$ and $TM_{RUR}$, respectively; Table 1). The stronger rural bias results in an average underestimation of $UHI_N$ by 0.6 K, with a 41-simulation average of 2.2 K [2 K – 2.3 K] vs. 2.8 K in the observation.





Accepted for publication in *Journal of Applied Meteorology and Climatology*. DOI 10.1175/JAMC-D-23-0145.1.

Every simulation but one (IPSL-CM5-A-MR—HIRHAM5) underestimates average $UHI_N$ with some variations between simulations and a stronger influence of the RCM than of the GCM. Besides average $UHI_N$ values, the ensemble tends to slightly overestimate small $UHI_N$ intensities and underestimate higher ones. All simulations but five (IPSL-CM5A-MR—HIRHAM5 and the four REMO2015 simulations) underestimate every percentile above the 25$^{th}$, and the whole ensemble has smaller values after the median. The underestimation of $UHI_N$ increases with greater intensities and is highest above the 90$^{th}$ percentile ($P_{90}$). The ensemble average of $P_{90}UHI_N$ is 1.6 K below the observed one (3.2 K [2.9 K – 3.5 K] vs. 4.6 K, Table 1). As with average JJA values, a positive, albeit smaller, bias in $TN_{RUR}$ is also found for summer days where $UHI_N$ is above the $P_{90}UHI_N$ (+0.8 K vs. +1.5 K; Table S5 in the online supplemental material), but the main difference is in urban areas where $TN_{URB}$ is underestimated (-1.1 K vs. +0.8 K).

In contrast to TN, cold biases are found for TX with similar magnitudes in the city and its surroundings (-0.8 K and -1.1 K, respectively). This results in a slight overestimation of $UHI_X$ of 0.3 K (0.8 K [0.7 K – 0.9 K]) that is much closer to the observation (0.5 K) than for $UHI_N$. All ensemble members, except for two RegCM4-6 simulations, overestimate $UHI_X$. The influence of the RCMs is less apparent than for $UHI_N$ and no clear pattern of a GCM or RCM doing better or worse is noted, with the exception of HIRHAM5 who systematically simulates higher $UHI_X$ (average bias 0.7 K), and RegCM4-6 who has lower $UHI_X$ than the ensemble (0.5 K vs 0.8 K) and is closer to the observation (bias 0 K). For the highest $UHI_X$ ($P_{90}$), unlike $UHI_N$ where biases increase with greater intensities, $P_{90}UHI_X$ biases remain similar to the average ones (0.3 K, Table 1).

Overall, the results of the whole SDD and SURFEX offline simulations chain are quite satisfactory. The RCMs simulate shortwave radiation and precipitation well with the latter being slightly overestimated. The underestimation of $UHI_N$ values is systematically due to a stronger positive bias observed over rural temperatures while $TN_{URB}$ is better simulated, their biases are less than 1 K; this is to be kept in mind if the results are to be used to analyze other impact indicators such as heat stress or building energy consumption over the city. $UHI_X$ are on average low to non-existent in the observation, which is well captured by the statistically-downscaled RCM ensemble.





Accepted for publication in *Journal of Applied Meteorology and Climatology*. DOI 10.1175/JAMC-D-23-0145.1.

## 4. Future climate projection of temperature and Urban Heat Island intensity

*a. Regional climate trends*

The SDD makes it possible to simulate the local effects of climate change on the Paris region, with spatial responses that may vary according to the elevation and land cover. Nonetheless, despite the spatial variability in temperature simulated by SURFEX, the evolution of rural background temperature in future climate is found on average consistent and comparable to the one simulated by the RCMs. For RCP4.5, the expected average annual warming between the periods 2080-2099 and 1976-2005 is +1.9 K [1.7 K – 2.2 K] for $TN_{RUR}$ and +2.0 K [1.7 K – 2.2 K] for $TX_{RUR}$. For RCP8.5, $TN_{RUR}$ increases by 3.6 K [3.2 K – 3.8 K] and $TX_{RUR}$ by 3.8 K [3.3 K – 4.5 K] (average warming is only 0.1 K higher in the 41 simulations ensemble, Fig. 4 and Table S6 in the online supplemental material). Seasonal differences of up to 1.8 K are observed in warming rates. They are more pronounced at the end of the century than in the near future, for RCP8.5 compared with RCP4.5 and for TX compared with TN (Cattiaux et al. 2015; Lindvall and Svensson 2015). Generally speaking, JJA (and sometimes SON) warm the most with 4.1 K [3.4 K – 4.7 K] for the 14 simulations $TN_{RUR}$ at the end of the century, and 4.8 K [3.9 K – 5.6 K] for $TX_{RUR}$. MAM warms the least, followed by DJF with 3.4 K [3.0 K – 3.8 K] for $TN_{RUR}$ and 3.3 K [2.9 K – 3.8 K] for $TX_{RUR}$ for RCP8.5.





Accepted for publication in *Journal of Applied Meteorology and Climatology*. DOI 10.1175/JAMC-D-23-0145.1.

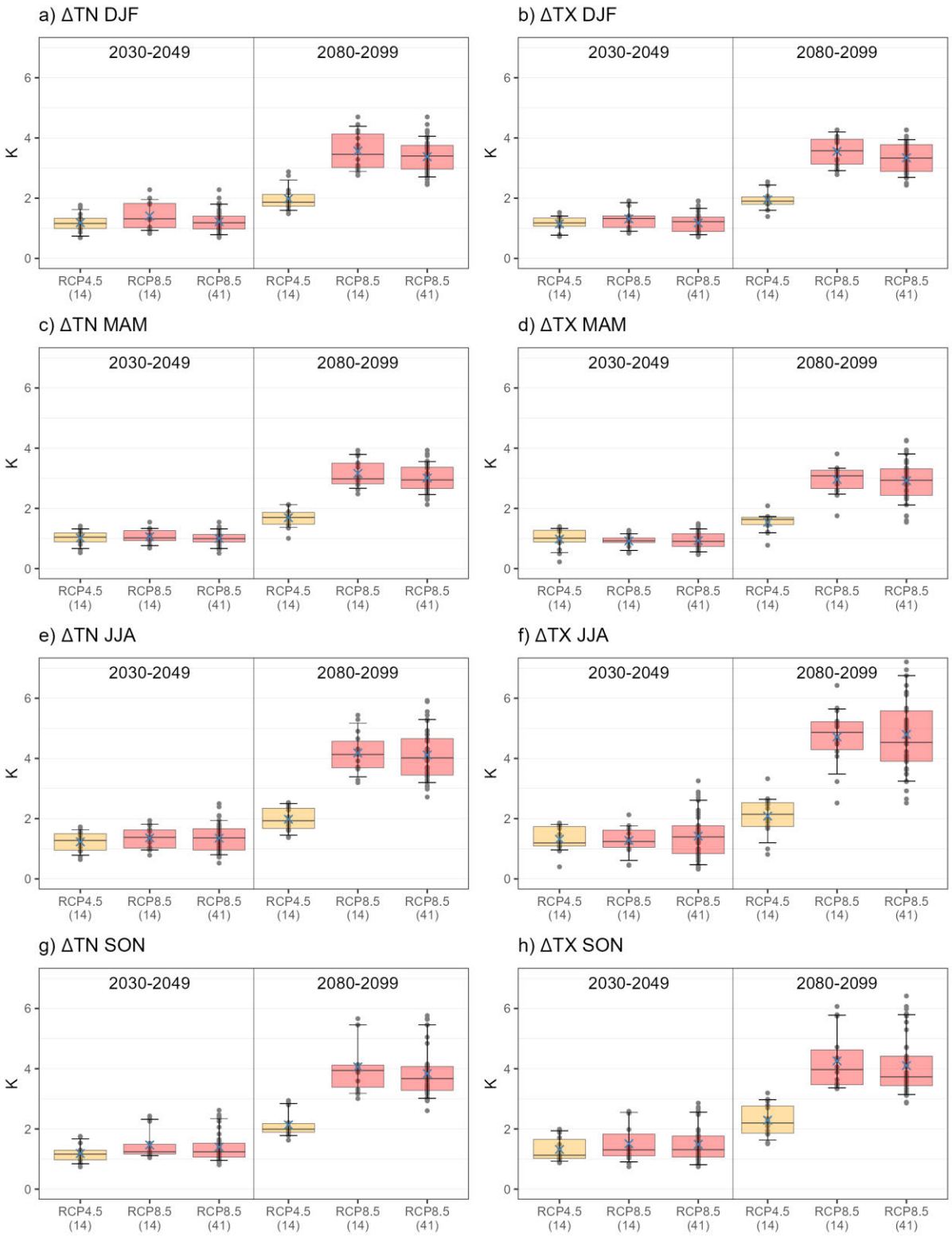


Fig. 4. Projected temperature change in the near and far future (2030–2049 and 2080–2099) in comparison to the historical period (1976-2005) for the RCP4.5 (orange) and RCP8.5 (red). The black dot represent each model. In addition to the mean (blue cross), the spread of the ensemble is represented by the percentiles 25 and 75 (boxplot) and whiskers (percentiles 10 and 90).





Accepted for publication in *Journal of Applied Meteorology and Climatology*. DOI 10.1175/JAMC-D-23-0145.1.

Previous studies have highlighted that the EURO-CORDEX RCMs project significantly less temperature increase than their driving CMIP5 GCMs (Boé et al. 2020, Gutiérrez et al. 2020), especially in summer with a future temperature increase over France that is more than 1 K lower than in the GCMs (Ribes et al. 2022). Sørland et al. (2018) have shown that non-EURO-CORDEX-RCMs could inverse the sign of temperature changes simulated by their driving GCMs over Europe. Even if some added-value of RCMs has been shown compared to GCMs (e.g. over mountainous or coastal areas, or when simulating extreme weather events) for the historical period (Rummukainen 2016, Sørland et al. 2018, Solman and Blázquez, 2019), the question of diverging trends between GCMs and RCMs remains open. Two hypotheses are put forward: (1) RCMs do not incorporate the temporal evolution of aerosols (Bartók et al. 2017; Boé et al. 2020, Gutiérrez et al. 2020), and (2) RCMs do not explicitly model the physiological effects of vegetation under changing atmospheric CO2 concentration (Schwingshackl et al. 2019, Boé et al. 2021). That should be kept in mind when comparing the results at the end of the century between the two scenarios, relative to the historical period or in relation to other studies that might be based on simulations with greater warming trends.

*b. Projected Urban Heat Island and urban temperature changes*

Rural areas exhibit a higher warming rate than urban areas. This is reflected by the temporal evolution of average UHI intensities. Focusing on JJA, Fig. 5 represents the evolution of average urban temperatures, average UHI intensities, and the 90$^{th}$ percentile of UHI intensities ($P_{90}$UHI); both at night and during the day. Over the 1976–2005 period, SURFEX simulates an average summer $UHI_N$ of 2.06 K on average [1.96 K – 2.13 K] (2.17 K [2.00 K – 2.30 K] for the 41 models; Table S7 in the online supplemental material). The most extreme $UHI_N$ ($P_{90}$) can reach 3.02 K [2.86 K – 3.11 K] (3.23 K [2.96 K – 3.5 K] for the 41 models; Table S8 in the online supplemental material). Because of the relatively small changes in UHI intensities compared to their natural variability over the historical period, i.e. less than 0.2 K compared to standard deviations of up to 1 K for $UHI_N$ (not shown), the significance of UHI changes is assessed using two-sample unpaired Wilcoxon-Mann-Whitney rank sum tests with continuity correction (Wilcoxon, 1945; Mann & Whitney 1947), with p.values smaller than 0.01.





Accepted for publication in *Journal of Applied Meteorology and Climatology*. DOI 10.1175/JAMC-D-23-0145.1.

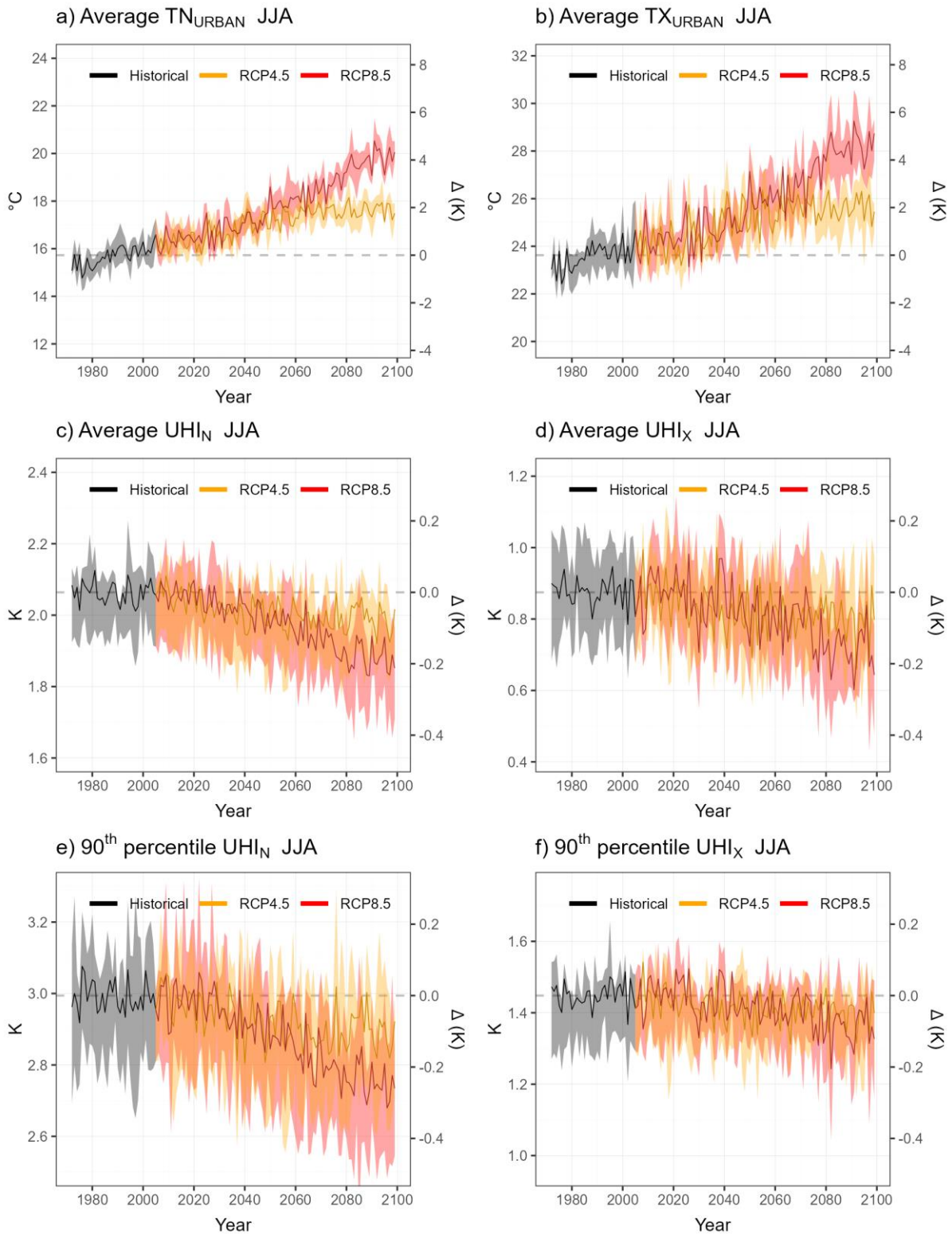


Fig. 5. Projected evolution of summer air temperature and UHI. (a) urban daily minimum temperature, (b) urban daily maximum temperature, (c) average nocturnal UHI intensity and (d) average diurnal UHI intensity, (e) 90$^{th}$ percentile of nocturnal UHI, (f) 90$^{th}$ percentile of diurnal UHI. The solid lines represent the average of the ensemble of 14 GCM/RCM couples common to the two RCP scenarios and the shaded areas represent their spread (25$^{th}$ and 75$^{th}$ percentiles). The horizontal lines represent the 1976–2005 averages.





Accepted for publication in *Journal of Applied Meteorology and Climatology*. DOI 10.1175/JAMC-D-23-0145.1.

From 2030–2049, small but significant changes in $UHI_N$ average intensities are found for 9 out of 14 models for both RCPs scenarios, with different models between the two scenarios. For RCP4.5, every model but two project a decrease of $UHI_N$ in JJA. Only CNRM-CM5—RACMO22E projects a significant increase of 0.08 K and CNRM-CM5-ALADIN63 a non-significant increase of 0.01 K. The average decrease of $UHI_N$ in the 14 simulations is -0.06 K [-0.11 K – -0.01 K] (Table S9 in the online supplemental material). For RCP8.5, CNRM-CM5—RACMO22E projects again a significant increase of 0.07 K, as does HadGEM2-ES—RACMO22E (+0.002 K, not significant), while the other 12 models project a decrease. The average decrease of $UHI_N$ in the 14 RCP8.5 simulations is -0.05 K [-0.08 K – -0.04 K]. The low $UHI_N$ differences between the two RCPs are explained by the fact that temperatures diverge only after the 2060s between these scenarios.

By 2080-2099, similar values of $UHI_N$ to 2030-2049 are found for RCP4.5. All simulations project a decrease of $UHI_N$, except CNRM-CM5—RACMO22E (+0.05 K, not significant [p.value 0.0109]) with 9 out of 13 having a significant decrease. The average decrease of the 14 simulations is -0.07 K [-0.11 K – -0.04 K]. For RCP8.5, the trend is intensifying in response to temperatures that continue to rise after the middle of the 21$^{th}$ century. All simulations except CNRM-CM5—RACMO22E (+0.01 K not significant) project significantly lower $UHI_N$ intensities. The average decrease of the 14 simulations is -0.19 K [-0.24 K – -0.14 K] (-0.22 K [-0.29 K – -0.13 K] taking 41 simulations). Summer $UHI_N$ values in 2080-2099 are 1.99 K [1.87 K – 2.03 K] for RCP4.5 and 1.88 K [1.74 K – 1.95 K] for RCP8.5 (1.95 K [1.84 K – 2.02 K] for the 41 simulations; Table S10 in the online supplemental material). The 41 simulations ensemble simulates a greater decrease of $UHI_N$ and higher end-of-century values than the 14 simulations ensemble because it starts with higher values over the historical period (+0.11 K). The extreme $UHI_N$ intensities ($P_{90}UHI_N$) decrease more (by -0.24 K [-0.31 K – 0.21 K] (-0.33 K [-0.22 K – -0.22 K]; Tables S11 and S12 in the online supplemental material) than the average ones leading to a change in the shape of the $UHI_N$ distribution with a less heavy tail of very high $UHI_N$. .

During the day, SURFEX simulates slightly higher urban than rural temperature, which leads to an average summer $UHI_X$ of 0.87 K [0.80 K – 0.94 K] (0.78 K [0.63 K – 0.90 K] for the 41 simulations) over the historical period. Similarly to $UHI_N$, $UHI_X$ decreases for the





Accepted for publication in *Journal of Applied Meteorology and Climatology*. DOI 10.1175/JAMC-D-23-0145.1.

majority of models in the near future: 12 out of 14 for RCP4.5 (the decrease is significant for 8 out of the 12 simulations) and 10 out of 14 for RCP8.5 (the decrease is significant for 6 out of the 10 simulations). Only HadGEM2-ES—RCA4 projects a significant increase of 0.04 K and 0.08 K in 2030-2049 for RCP4.5 and RCP8.5, respectively; the other increases are not significant. The $UHI_X$ decrease is on average -0.05 K [-0.08 K – -0.02 K] for RCP4.5 and -0.03 K [-0.08 K – 0.00 K] for RCP8.5 (-0.04 K [-0.09 K – 0.00 K] for the 41 simulations).

In 2080-2099, for RCP4.5, 11 of the 14 simulations project a decrease of $UHI_X$. The other 3 are HadGEM2-ES—RACMO22E, CNRM-CM5—RCA4, and HadGEM2-ES—RCA4, which project increases of 0.04 K, 0.03 K, and 0.04 K, respectively. The ensemble average decrease of $UHI_X$ is -0.07 K [-0.12 K – -0.05 K]. For RCP8.5, all simulations project a significant decrease of $UHI_X$, except for the CNRM-CM5—RACMO22E simulation which projects a non-significant decrease; the ensemble average $UHI_X$ decrease is -0.16 K [-0.22 K – -0.09 K] (-0.16 K [-0.23 K – -0.07 K] for the 41 simulations). Unlike for $UHI_N$, the more extreme $UHI_X$ intensities ($P_{90}UHI_X$) do not decrease more than the average ones, but by half as much: -0.08 K [-0.10 K – -0.02 K]. At the end of the century, summer $UHI_X$ intensities are 0.80 K [0.70 K – 0.89 K] for RCP4.5 and 0.71 K [0.60 K – 0.81 K] for RCP8.5 (0.63 K [0.46 K – 0.75 K] for the 41 simulations).

As noted by previous studies (Doblas-Reyes et al. 2021), the projected evolution of UHI intensities, when changes in urbanization are not taken into account, is an order of magnitude smaller than the regional climate warming and nighttime UHI intensities remain positive. Consequently, these changes do not represent an improvement of thermal conditions in the city. At the end of the century, the SURFEX simulations project that the maximum of $TX_{JJA}$ could reach up to 27.4 °C [25.8 °C – 28.4 °C] for RCP4.5 (Table S13 in the online supplemental material) and 30.2 °C [29.1 °C – 31.1 °C] for RCP8.5 at night ($TN_{URB}$), and 40.2 °C [37.7 °C – 41.9 °C] and 43.9 °C [40.8 °C – 46.5 °C] during the day ($TX_{URB}$); with the maximum of the ensemble drawing near the 50 °C threshold (49.5 °C by RCA4 driven by IPSL-CM5A-MR).

The projected UHI decreases may result from a divergent response of urban and rural areas to changing climate forcings. To clarify the mechanisms involved, changes in temperature patterns over the region are investigated.

Fig. 6.a represents the ensemble average summer $UHI_N$ maps for the historical period, i.e. the difference between air temperature at each point and the average rural temperature (Fig.





Accepted for publication in *Journal of Applied Meteorology and Climatology*. DOI 10.1175/JAMC-D-23-0145.1.

S2 in the online supplemental material for the 41 ensemble maps). During the historical period, the highest TN match the most urbanized areas with values being 2.6 K above the rural temperature at some grid points. Urban effects are combined with a regional warming gradient from the north-west to the south-east, found in all simulations with only varying magnitudes. The maps of $UHI_N$ differences projected at the end of the century for both scenarios (Fig. 6.c,e) show that the south-east of the domain warms faster than the north-west of the domain and also faster than the city. The difference in warming rates is quite small but apparent in most simulations. It is up to 0.1 K for RCP4.5 and 0.18 K for RCP8.5 between 2080–2099 and 1976–2005. On the other hand some parts of the city warm 0.3 K less than the rural areas for RCP8.5.

During the day (Fig. 6.b), the historical regional temperature gradient is less pronounced, and the urban-rural contrasts smaller. The same areas that are warming faster at night also warm faster during the day, but the magnitude of the warming rate is smaller. For both night and day, a small transition area appears in the south-west—north-east diagonal of the domain (points in Fig. 6.c to 5.f) where the simulations do not agree on the sign of the temperature change (less than 2/3 of the models).

To understand the reason behind the intensification of the regional temperature contrasts, the changes in LWT occurrence frequencies, in summer precipitation, in the soil moisture content, and in the surface energy balance are investigated.





Accepted for publication in *Journal of Applied Meteorology and Climatology*. DOI 10.1175/JAMC-D-23-0145.1.

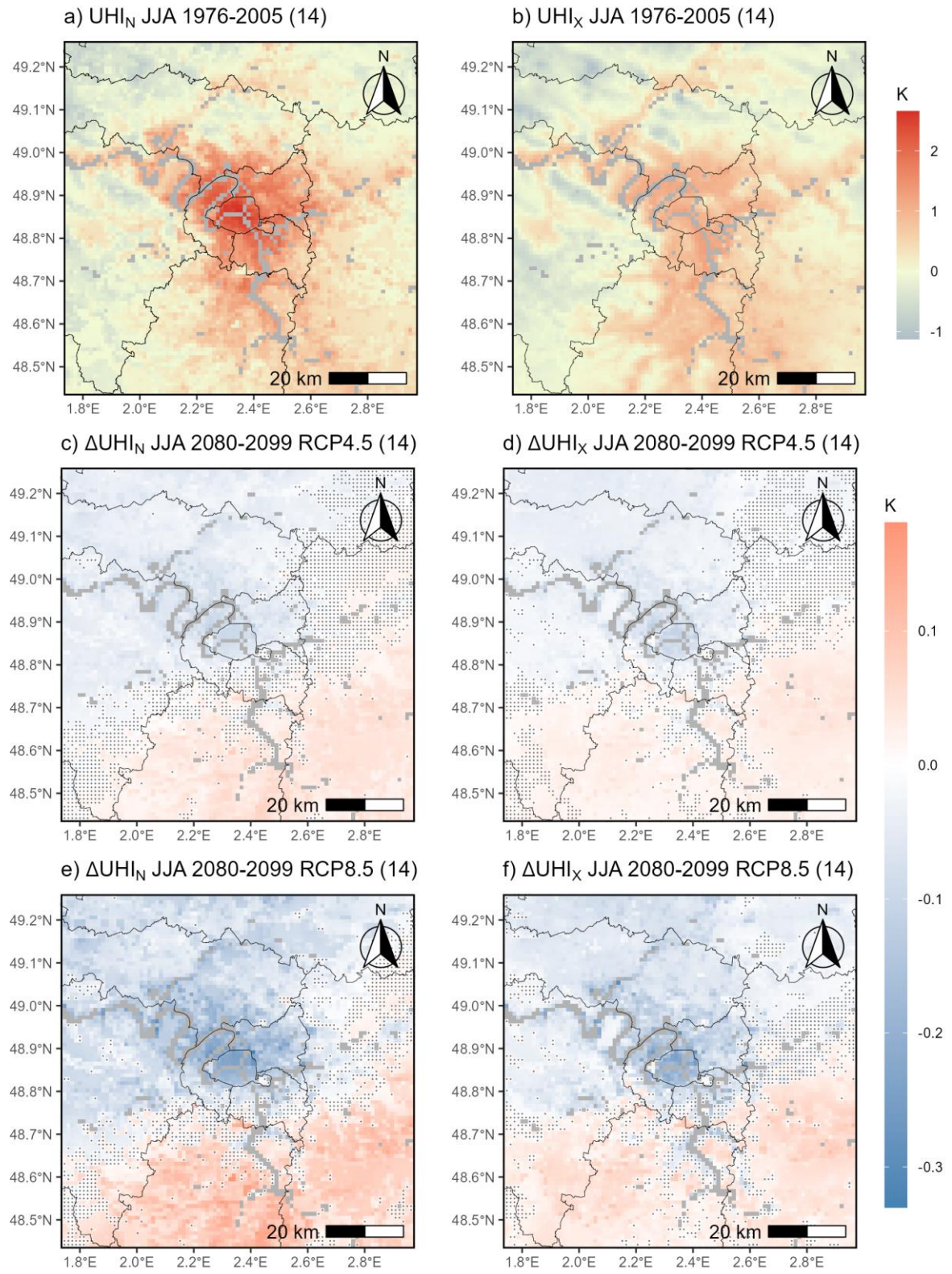


Fig. 6. Average seasonal $UHI_N$ and $UHI_X$ maps for JJA over the historical period 1976–2005 and differences in 2080–2099 for scenarios RCP4.5 and RCP8.5 and the 14 simulations. Daily UHI maps are obtained by subtracting $TN_{RUR}$/$TX_{RUR}$ from the temperature field. The gray areas represent points with more than 5% water body coverage that are removed. The





Accepted for publication in *Journal of Applied Meteorology and Climatology*. DOI 10.1175/JAMC-D-23-0145.1.

gray dots represent points where less than 66% of the models (10/14) agree on the sign of the change.

## 5. Investigation of physical mechanisms potentially explaining the projected UHI decrease

Multiple studies have looked at the projected evolution of UHIs around the globe, using GCMs (McCarthy et al. 2010; Oleson et al. 2011; 2012; Fischer et al. 2012), RCMs (McCarthy et al. 2012; Hamdi et al. 2015; Lauwaet et al. 2015a; Lauwaet et al. 2015b; Zhao et al. 2018; Sharma et al. 2019; Lo et al. 2020), Convection Permitting Models (CPM; Keat et al. 2021; Keppas et al. 2021; Lind et al. 2022), LSMs (Lemonsu et al. 2012; Hamdi et al. 2014; Nogueira et al. 2020; Duchêne et al. 2022) and statistical downscaling methods (Hatchett et al. 2016; Sachindra et al. 2016; Hoffmann et al. 2018). They project different trends depending on the area of the globe (i.e. climatic region) and the city. Results are sensitive to the approach used (dynamical versus statistical downscaling) but nevertheless show small UHI changes when compared to the regional warming: between less than a degree (Lauwaet et al. 2015b) to 1 K (Zhao et al. 2018). Several hypothesis have been put forward to explain the relatively small changes of UHI over the 21$^{th}$ century. Oleson et al. (2011) explain the decrease of $UHI_N$ around the world by an increased amount of long-wave radiation coming from higher future temperatures, which warms rural areas more than urban areas because of different ground heat storage capacities (Oleson et al. 2011; 2012; Fischer et al. 2012). Furthermore, Lauwaet et al. (2015b) noted that at night, due to stronger thermal inversions over rural areas, the extra heat is trapped closer to the surface, whereas over the city more mixing occurs and energy is distributed over a greater vertical extent. Lemonsu et al. (2012), Lo et al. (2020), and Keat et al. (2021) attributed the UHIs changes to drier soils in the future climate, which is due to changes in spring/summer precipitation and increased temperature.

### *a. Projected future change of local weather types*

An aspect little investigated by previous studies is a potential change in weather patterns that might influence the UHI evolution. Ozturk et al. (2021) have shown that the EURO-CORDEX ensemble projects small changes in summer wind fields over Europe but with a





Accepted for publication in *Journal of Applied Meteorology and Climatology*. DOI 10.1175/JAMC-D-23-0145.1.

significant increase in mean sea level pressure over the northern Atlantic with a strengthening of the Azores anticyclone, which could increase the occurrence frequencies of LWTs associated with wind coming from the North. Additionally, Røste and Landgren (2022) noted a significant increase of north-westerly flows for half of the ensemble members, a decrease of the Central-Eastern European high, the Scandinavian low and of south-southeasterly flow in summer.

In this study, the 14 simulations ensemble simulates a systematic increase of the frequency of LWT12 (north-east; +13% [7% – 18%]) and LWT9 (north-west; +8% [6% – 10%]) for RCP8.5 (+6% [5% – 8%] and +4% [3% – 5%] for RCP4.5), which are associated to medium and high $UHI_N$, respectively, (Le Roy et al. 2021). This could lead to an increase of $UHI_N$ in the future. Changes in atmospheric temperature fields at 50 m above the surface (built with the SDD) between 1976-2005 and 2080-209 are shown in Fig. 7 for summer at 3 UTC (Fig. S3 in the online supplemental material for the 41 ensemble maps). In contrast to near-surface temperature presented in Fig. 6, there is no change over the city, only an intensification of the regional gradient is found. The same is observed during the day (15 UTC, Fig. 7.d,f). Consequently it appears that the change of LWT frequencies is not responsible for the UHI changes projected in the future, at least not via its effect on the air temperature forcing.





Accepted for publication in *Journal of Applied Meteorology and Climatology*. DOI 10.1175/JAMC-D-23-0145.1.

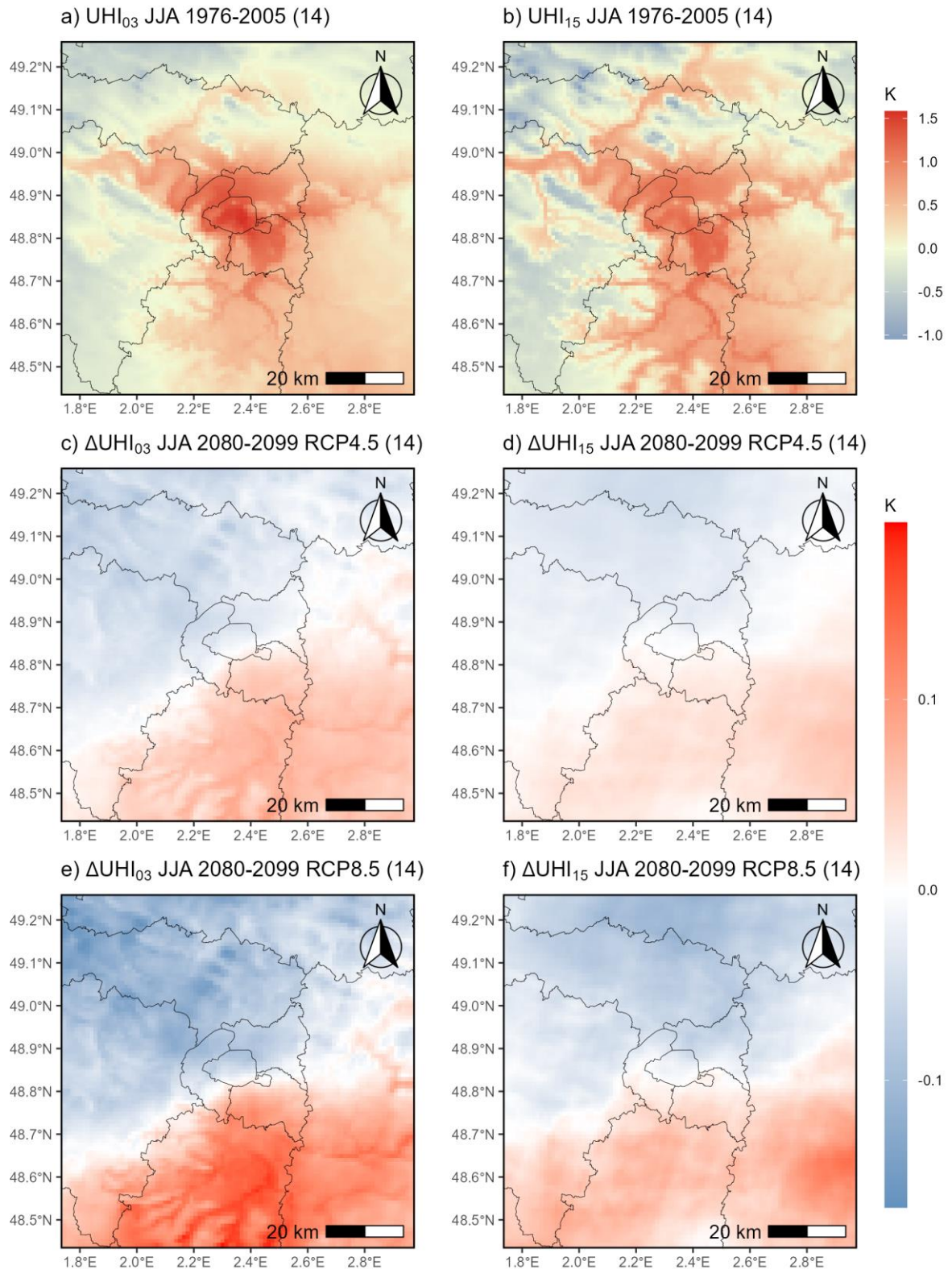


Fig. 7. Average seasonal forcing UHI maps (50 m) at 03 UTC and 15 UTC for JJA over the historical period 1976–2005 and differences in 2080–2099 for scenarios RCP4.5 and RCP8.5 and the 14 simulations.





Accepted for publication in *Journal of Applied Meteorology and Climatology*. DOI 10.1175/JAMC-D-23-0145.1.

b. Future evolution of precipitation and soil moisture

Lemonsu et al. (2012), Lo et al. (2020), and Keat et al. (2021) also found that future temperature increases faster in rural areas than in the city and hypothesized that it could be due to a decrease in the soil moisture content in the future because of decreasing precipitation in spring and summer. Projections of precipitation over France show uncertain evolution during the winter but significant decrease during the summer associated with increased risks of droughts (Spinoni et al. 2018). The EURO-CORDEX ensemble average projects a decrease in average daily rainfall for JJAS at the end of the 21$^{th}$ century for both scenarios, that is the most pronounced in July and August and greater for RCP8.5 than for RCP4.5. Some models project a decrease during JJA following a maximum in May, while the others project a later driest period extending to September. Focusing only on JA, the ensemble average (14 simulations) decreases by 30% [-39% – -25%] (from 2.2 mm.day$^{-1}$ [1.8 mm.day$^{-1}$ – 2.5 mm.day$^{-1}$] to 1.6 mm.day$^{-1}$ [1.1 mm.day$^{-1}$ – 1.7 mm.day$^{-1}$]).

The precipitation from the RCMs is applied uniformly over the SURFEX domain, without downscaling. However, its seasonal variability and its evolution with climate change can impact the soil moisture content simulated by SURFEX. Fig. 8 shows the yearly cycle of the amount of liquid water in the ground (WG) simulated by SURFEX for all natural areas surrounding the city. It follows the seasonal cycle of precipitation with maximum amounts in winter (around 36%) and minimum at the end of the summer (around 28%). In DJF, WG is almost identical across simulations. The soil is saturated and $WG_{DJF}$ is insensitive to the differences in precipitation between the RCMs. During JJA, WG is lower due to decreasing precipitation and increasing demand from vegetation for evapotranspiration. The evolution of WG follows that of precipitation with a one-month lag for all simulations, except for CNRM-CM5—RCA4. The average decrease of $WG_{JJA}$ is -0.7% [-1.3% – -0.1%] (from 28.5% [27.3% – 29.5%] to 27.8% [27.4% – 27.9%]) for RCP4.5 compared to -1.5% [-2.1% – -0.8%] (from 28.5% [27.3% – 29.5%] to 27% [26.4% – 27.7%]) for RCP8.5. All simulations simulate a decrease of $WG_{JJA}$, except for CNRM-CM5—KNMI-RACMO22E, which, in contrast to all other models simulates an increase of MJJAS precipitation. This leads to a much smaller $WG_{JJA}$ decrease of -0.8% and -0.1% for RCP4.5 and RCP8.5, respectively.





Accepted for publication in *Journal of Applied Meteorology and Climatology*. DOI 10.1175/JAMC-D-23-0145.1.

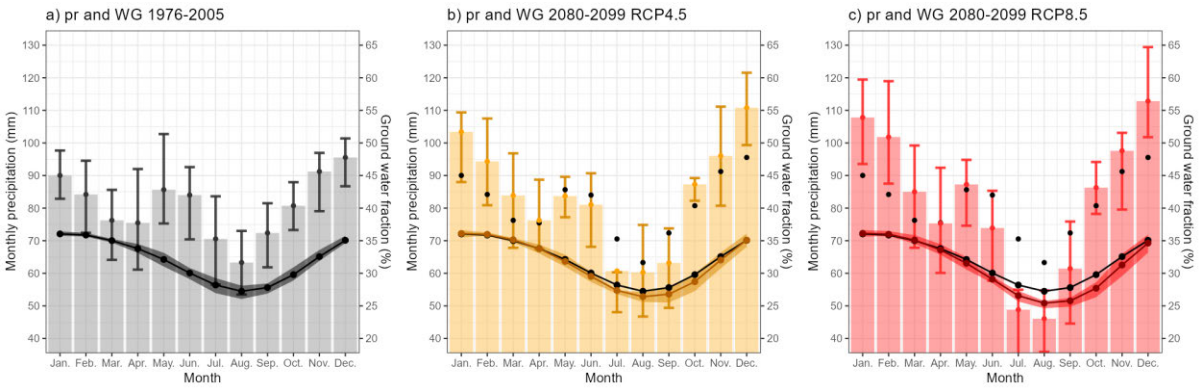


Fig. 8. Historical (a) and future monthly precipitation amounts and fractions of ground water for RCP4.5 (b) and RCP8.5 (c). Barplot represent the ensemble average of monthly precipitation, error bars the spread of the ensemble (interquartile range). The line represent the ensemble average of ground water fraction and the shaded area the spread of the ensemble. Historical values are also represented on the future plots (black).

c. Future evolution of the summer Surface Energy Balance

The amount of energy received by the surface is expected to be altered in the future due to changes in incoming long-wave radiation (L↓) associated with higher air temperature and possible changes in incoming shortwave radiation (S↓) resulting from evolution of cloud cover conditions or aerosols, although their evolution through the 21$^{th}$ century might not be well represented by the CORDEX RCMs (Boé et al. 2020). Even with more upwelling long-wave radiation (L↑) – enhanced by higher future surface temperatures – all simulations project greater net allwave radiation (Q*) for 2080-2099 than for1976-2005. The different ways this additional energy is distributed between sensible heat ($Q_H$), latent heat ($Q_E$) and ground heat ($Q_G$), as well as the difference between urban and rural response, could explain the projected UHI evolution.

The future changes in S↓ and S↑ come from RCMs only because the SDD is not applied to these variables and because the land cover does not evolve during the whole period (no changes in albedo). S↓ in the 14 RCMs increases by 13 W.m$^{-2}$ [5.9 W.m$^{-2}$ – 18.2 W.m$^{-2}$] from 226 W.m$^{-2}$ [210 W.m$^{-2}$ – 241 W.m$^{-2}$] to 239 W.m$^{-2}$ [221 W.m$^{-2}$ – 256 W.m$^{-2}$] for RCP8.5. L↓ is also taken from the RCMs but is modified by the SDD which takes into account the modification of the air temperature above the canopy by the city and keeps the original apparent air emissivity of the RCMs (Unsworth & Monteith, 1975; Sedlar & Hock 2009). Because of higher air temperature, L↓ simulated by the RCMs is projected to increase by 26.6 W.m$^{-2}$ [23.5 W.m$^{-2}$ – 27.1 W.m$^{-2}$] from 349 W.m$^{-2}$ [347 W.m$^{-2}$ – 352 W.m$^{-2}$]. The





Accepted for publication in *Journal of Applied Meteorology and Climatology*. DOI 10.1175/JAMC-D-23-0145.1.

contribution induced by the local warming derived from the SDD should only represent a few W $m^{-2}$ because the increase in air temperature forcing resulting from a change in LWT frequencies in SDD remains less than 0.3 K on average.

Table 3 compiles average summer components of the SEB for 1976–2005 and 2080–2099 for RCP8.5 both in urban and rural areas (Fig. 9). Historical $UHI_N$ intensities come from the combination of (1) greater $Q_G$ values (urban-rural difference of +7.9 W.m-2 [7.7 $W.m^{-2}$ – 10.3 $W.m^{-2}$]) over the city (35 $W.m^{-2}$ [33 $W.m^{-2}$ – 40 $W.m^{-2}$]) than over rural areas (27 $W.m^{-2}$ [25 $W.m^{-2}$ – 30 $W.m^{-2}$]), (2) higher $Q_H$ values (urban-rural difference of 38.2 $W.m^{-2}$ [35.7 $W.m^{-2}$ – 41.8 $W.m^{-2}$]) – that include anthropogenic fluxes ($Q_F$), and (3) conversely lower $Q_E$ (urban-rural difference of -45.4 $W.m^{-2}$ [-52.2 $W.m^{-2}$ – -40.0 $W.m^{-2}$]). This highlights the greater capacity of the city to capture heat during the day and restore it during the night thus limiting the cooling of the air near the surface and its lower ability to cool through evaporative processes (Nunez and Oke, 1977).

| | | $Q_H$ ($W.m^{-2}$) | $Q_E$ ($W.m^{-2}$) | $Q_G$ ($W.m^{-2}$) | $\beta = Q_H / Q_E$ |
|---|---|---|---|---|---|
| 1976-2005 | Urb | 98 [89 – 109] | 84 [75 – 94] | 35 [33 – 40] | 1.17 |
| | Rur | 60 [47 – 69] | 129 [115 – 145] | 27 [25 – 30] | 0.46 |
| | Dif | 38.2 [35.7 – 41.8] | -45.4 [-52.2 – -40] | 7.9 [7.7 – 10.3] | 0.71 |
| 2080-2099 RCP8.5 | Urb | 119 [110 – 134] | 75 [62 – 87] | 43 [37 – 50] | 1.59 |
| | Rur | 81 [71 – 98] | 116 [97 – 135] | 31 [26 – 35] | 0.70 |
| | Dif | 37.4 [34.1 – 40.6] | -41.4 [-48.6 – -35] | 12.4 [11.2 – 15.6] | 0.89 |
| Difference | Urb | 20.2 [11.4 – 30.3] | -9.1 [-14.2 – -2.9] | 8.1 [7.5 – 9.8] | 0.42 |
| | Rur | 21.1 [10.2 – 32.2] | -13.1 [-19.6 – -5.8] | 3.6 [2.7 – 4.8] | 0.24 |
| | Dif | -0.8 [-2.2 – 1.7] | 4 [1.9 – 5.9] | 4.5 [3.5 – 5.4] | 0.18 |

Table 2. Summer ensemble average (and interquartile range) of the components of the Surface Energy Balance over urban and rural areas for the historical period 1976-2005 and





Accepted for publication in *Journal of Applied Meteorology and Climatology*. DOI 10.1175/JAMC-D-23-0145.1.

the end of the century 2080-2099 (under RCP8.5). Are also presented the difference between urban and rural areas, as well as the difference between the two periods.

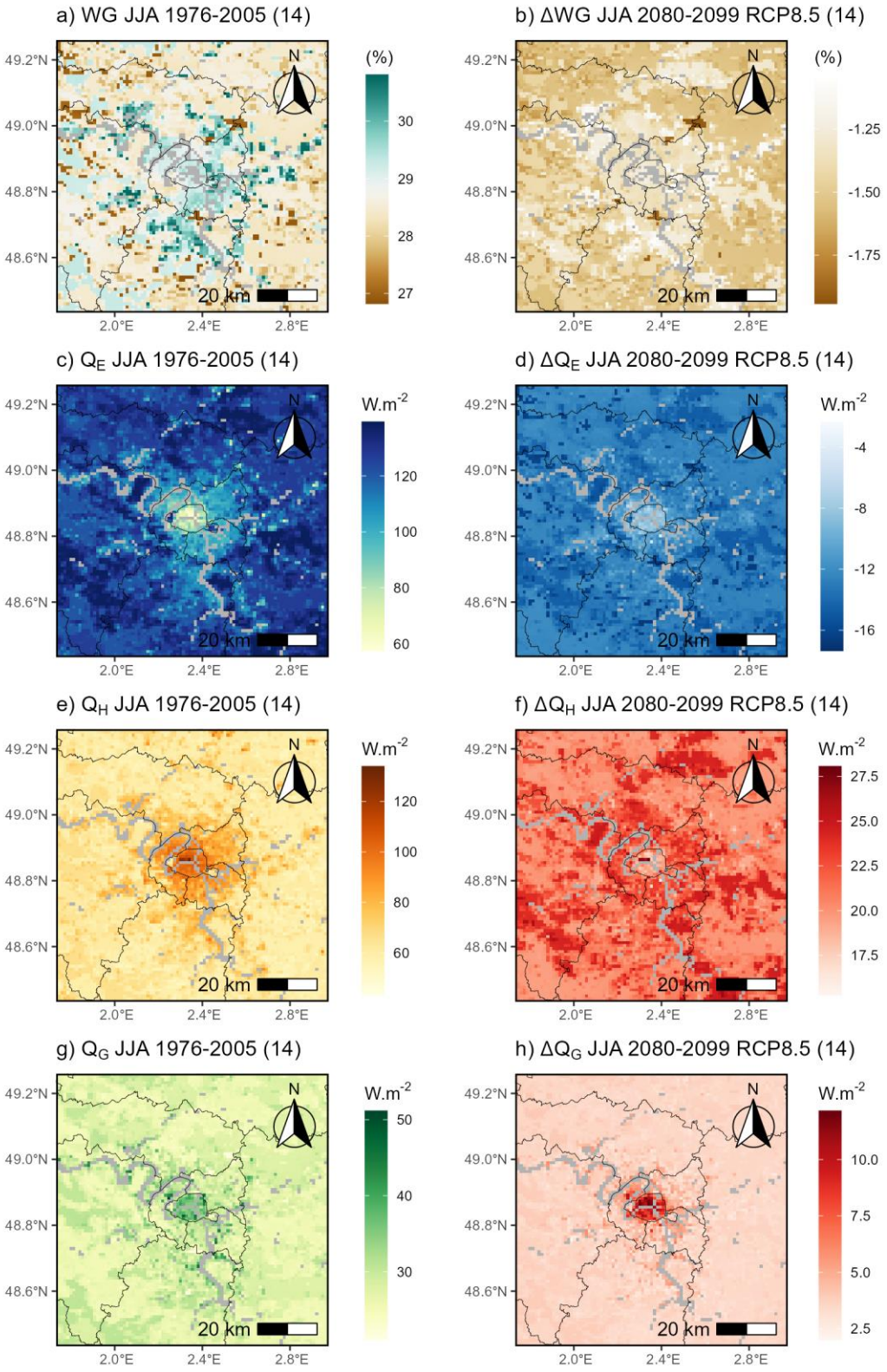






Accepted for publication in *Journal of Applied Meteorology and Climatology*. DOI 10.1175/JAMC-D-23-0145.1.

Fig. 9. Average seasonal maps for JJA over the historical period 1976–2005 and change in the future for RCP8.5 for soil water content (WG, a, b), latent heat flux (QE, c, d), sensible heat flux (QH, e, f) and ground heat flux (QG, g, h)

Summer $UHI_N$ and $UHI_X$ intensities are produced by different mechanisms as can be seen by the absence of a significant correlation between them over the historical period (not shown). Since there is also no significant correlation between their changes in future climate ($\Delta UHI_N$ and $\Delta UHI_X$), it is therefore expected that their change in the future is also governed by different physical processes. Fig. 10 represents average changes in summer UHIs and their relation to changes in other variables. $\Delta UHI_N$ is most correlated to $\Delta LW_{RCM}$ (a) at least for RCP8.5 ($r^2 = 0.32$; p.value < 0.05) in agreement with Oleson et al. (2011) and Lauwaet et al. (2015b)'s findings. During the day (e), the inverse effect is noted for RCP4.5 ($r^2 = 0.31$; p.value < 0.05); the main drivers are $\Delta Q_{H,URB}$ (f) and $\Delta Q_{E,URB}$ (g). Over the whole domain, $Q_H$ is expected to increase at the expense of $Q_E$, because of the projected decrease of WG associated with lower precipitation, resulting in an increase of the Bowen ratio ($\beta = Q_H / Q_E$). $\beta_{JJA}$ increases more in absolute terms in the urban areas than in the rural surroundings (+0.42 vs. +0.24, see Table 3), but in relative terms, it increases by 52% in rural areas comparing to 36% in urban areas. Similarly to Oleson et al. 2011, 2012 and Fischer et al. 2012's findings, the increase of LW is also linked to increasing $Q_G$ in the future, both over urban and rural areas. Even at the end of the century, $Q_{G,URB}$ remains greater than $Q_{G,RUR}$ and so do $\Delta Q_{G,URB}$ and $\Delta Q_{G,RUR}$ (both in absolute or relative terms), which should in theory translate to an increase of $UHI_N$ (because of more heat being stored during the day in the city and released at night). Nevertheless, some of the simulations projecting the greatest increase in $Q_G$ are also those with the greatest decrease of WG (d, h). Consequently, while $TN_{URB}$ is expected to increase because of the release of $Q_G$ at night, $TN_{RUR}$ increases faster because the soil dries out, reducing the cooling potential through evapotranspiration of the vegetation.





Accepted for publication in *Journal of Applied Meteorology and Climatology*. DOI 10.1175/JAMC-D-23-0145.1.

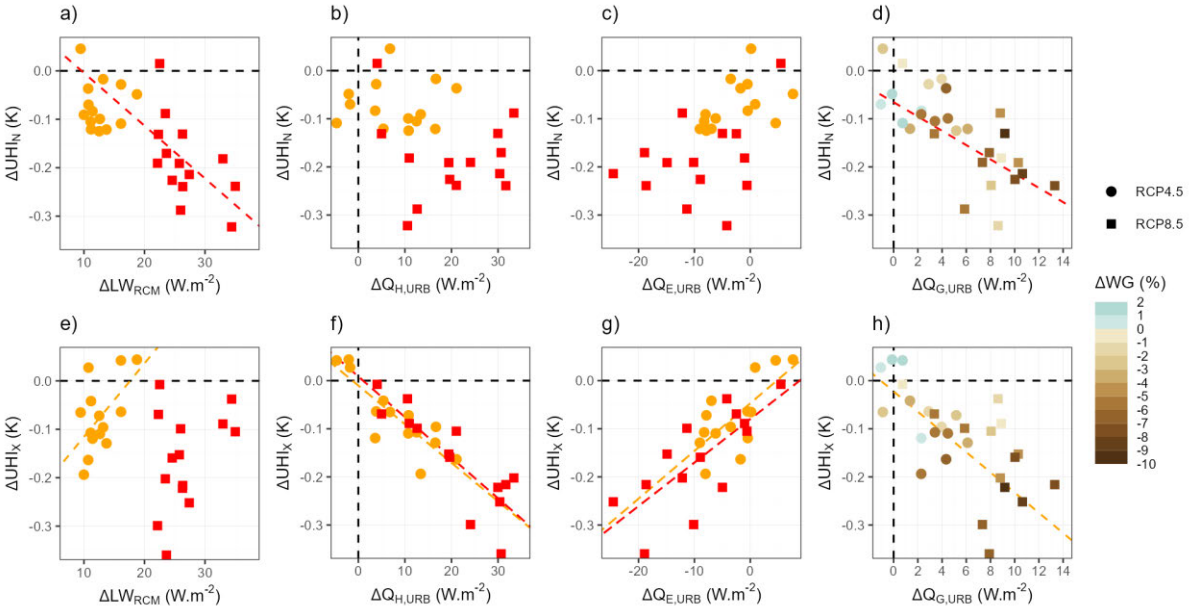


Fig. 10. Potential drivers of summer Urban Heat Island intensities change at the end of the century (2080-2099) compared with the historical period (1976-2005) for two emission scenarios (RCP4.5, orange circles and RCP8.5 red squares). Rows: nighttime and daytime summer Urban Heat Island intensities. Columns: all hours downwelling long-wave radiation (a,e), daytime urban sensible heat flux (b,f), daytime urban latent heat flux (c,g), daytime urban ground heat flux and all hours rural ground water content (d,h). Linear regression lines are displayed when significant ($0.01 < p.value < 0.05$).

## 6. Conclusion

The statistical-dynamical downscaling approach developed by Le Roy et al (2021) has been applied to the large ensemble of EURO-CORDEX regional climate projections for the two RCP4.5 and RCP8.5 scenarios to refine them to the urban agglomeration scale by adding the impact of the city of Paris on the regional climate simulated by the RCMs. These forcings are used to drive the SURFEX land surface model coupled to the TEB urban canopy model in order to carry out simulations at 1 km resolution over the Île-de-France administrative region and the period 1970-2099.

The urban simulations have been evaluated against different datasets taking account of urbanization, especially for air temperature. Similar biases than those inherited from the RCMs have been found in the downscaled data, with TN too high and TX too low. More importantly, different biases have been found for the city and its surroundings, resulting in an underestimation of $UHI_N$ of 0.6 K and an overestimation of $UHI_X$ of 0.3 K (-1.4 K and +0.3 K for the 90$^{th}$ percentiles). Changes in TN and TX are then analyzed over the century





Accepted for publication in *Journal of Applied Meteorology and Climatology*. DOI 10.1175/JAMC-D-23-0145.1.

focusing on the two periods 2030-2049 and 2080-2099. In the near future, $TN_{URB}$ and $TX_{URB}$ are expected to increase in similar proportions for both scenarios. At the end of the century, there are greater differences in warming between TN and TX and between the scenarios. The season with the greatest warming is JJA for TN (4.0 K) and TX (4.6 K). The rural warming is almost identical to that predicted by the RCM on average, but important spatial variations and urban-rural contrasts are noted. In JJA, urban warming is weaker than rural warming for TN and TX, resulting in a significant decrease in $UHI_N$ and $UHI_X$ of -0.19 K and -0.16 K, respectively for RCP8.5 in 2080-2099. Various mechanisms have been studied to explain these changes. The impacts of the change in mesoscale circulation already noted by previous studies and their impact on local weather conditions were found to have an effect on regional temperatures with an intensification of a north-west to south-east gradient, but not in the city. Future summer rainfall decreases in the RCMs, leading to a decrease in soil moisture content, but none of the variables or their future change were correlated with $UHI_N$ (unlike $UHI_X$). All RCMs project an increase in net radiation and ground heat flux in urban areas, which could potentially lead to an increase in $UHI_N$. However, this is counterbalanced by lower soil moisture in rural areas leading to a stronger increase of rural air temperature compared to urban air temperature. Two different processes are found to compensate each other: on the one hand, the increase of ground heat flux due to a greater amount of incoming shortwave radiation and, on the other, the decrease in precipitation leading to lower soil moisture values. This could explain the difficulty of previous studies in agreeing on the sign of change in future UHIs around the world when looking at different cities or using different approaches.

Nevertheless, as noted by previous studies, the decrease of $UHI_N$ is an order of magnitude smaller than the projected increase of regional air temperature and urban areas remain warmer than rural ones in the future. At the end of the 21$^{st}$ century, the JJA-averaged urban temperatures could reach up to almost 20 °C at night (19.7 °C) and close to 30 °C during the day (28.2 °C).

The high-resolution urban simulations carried out as part of this study have made it possible to analyze the expected changes in temperature and UHIs in the future, but they will also be used to study various impacts of climate change in Paris, such as changes in the thermal comfort of residents (via the Universal Thermal Climate Index, UTCI) or changes in the energy consumption of buildings due to heating and cooling.





Accepted for publication in *Journal of Applied Meteorology and Climatology*. DOI 10.1175/JAMC-D-23-0145.1.

*Acknowledgments.*

The authors would like to thank the research institutes involved in the EURO-CORDEX initiative.

*Data Availability Statement.*

All EURO-CORDEX regional climate projections used in this study are openly available from the Earth System Grid Federation at https://esgf-data.dkrz.de/projects/esgf-dkrz/.

REFERENCES

Aguejdad, R., Doukari, O., Houet, T., Avner, P., & Viguié, V. (2016). Etalement urbain et géoprospective: apports et limites des modèles de spatialisation. Application aux modèles SLEUTH, LCM et NEDUM-2D. *Cybergeo: European Journal of Geography*.

Arnfield, A. J. (2003). Two decades of urban climate research: a review of turbulence, exchanges of energy and water, and the urban heat island. International Journal of Climatology: a Journal of the Royal Meteorological Society, 23(1), 1-26.

Bartók, B., Wild, M., Folini, D., Lüthi, D., Kotlarski, S., Schär, C., ... & Imecs, Z. (2017). Projected changes in surface solar radiation in CMIP5 global climate models and in EURO-CORDEX regional climate models for Europe. *Climate dynamics*, *49*, 2665-2683.

Bernard, É., Munck, C. D., & Lemonsu, A. (2022). Detailed Mapping and Modeling of Urban Vegetation: What Are the Benefits for Microclimatic Simulations with Town Energy Balance (TEB) at Neighborhood Scale?. *Journal of Applied Meteorology and Climatology*, *61*(9), 1159-1178.

Bocher, E., Petit, G., Bernard, J., & Palominos, S. (2018). A geoprocessing framework to compute urban indicators: The MApUCE tools chain. *Urban climate*, *24*, 153-174.

Boé, J. (2021). The physiological effect of CO2 on the hydrological cycle in summer over Europe and land-atmosphere interactions. *Climatic Change*, *167*(1), 1-20.

Boé, J., Somot, S., Corre, L., & Nabat, P. (2020). Large discrepancies in summer climate change over Europe as projected by global and regional climate models: causes and consequences. *Climate Dynamics*, *54*(5), 2981-3002.

Boé, J., Terray, L., Habets, F., & Martin, E. (2006). A simple statistical-dynamical downscaling scheme based on weather types and conditional resampling. Journal of Geophysical Research: Atmospheres, 111(D23).

Bueno, B., Pigeon, G., Norford, L. K., Zibouche, K., & Marchadier, C. (2012). Development and evaluation of a building energy model integrated in the TEB scheme. *Geoscientific model development*, *5*(2), 433-448.

Buzan, J. R., & Huber, M. (2020). Moist heat stress on a hotter Earth. Annual Review of Earth and Planetary Sciences, 48, 623-655.

Canellas, C., Gibelin, A. L., Lassègues, P., Kerdoncuff, M., Dandin, P., & Simon, P. (2014). Les normales climatiques spatialisées Aurelhy 1981-2010: températures et précipitations. *La météorologie*.

Cattiaux, J., Douville, H., Schoetter, R., Parey, S., & Yiou, P. (2015). Projected increase in diurnal and interdiurnal variations of European summer temperatures. *Geophysical Research Letters*, *42*(3), 899-907.

Champeaux, J. L., Masson, V., & Chauvin, F. (2005). ECOCLIMAP: a global database of land surface parameters at 1 km resolution. *Meteorological Applications: A journal of forecasting, practical applications, training techniques and modelling*, *12*(1), 29-32.

Chapman, S., Watson, J. E., Salazar, A., Thatcher, M., & McAlpine, C. A. (2017). The impact of urbanization and climate change on urban temperatures: a systematic review. *Landscape Ecology*, *32*, 1921-1935.

Chen, F., Bornstein, R., Grimmond, S., Li, J., Liang, X., Martilli, A., ... & Wang, Y. (2012). Research priorities in observing and modeling urban weather and climate. Bulletin of the American Meteorological Society, 93(11), 1725-1728.

Daniel, M., Lemonsu, A., Déqué, M., Somot, S., Alias, A., & Masson, V. (2019). Benefits of explicit urban parameterization in regional climate modeling to study climate and city interactions. Climate Dynamics, 52(5-6), 2745-2764.

Dixon, K. W., Lanzante, J. R., Nath, M. J., Hayhoe, K., Stoner, A., Radhakrishnan, A., ... & Gaitán, C. F. (2016). Evaluating the stationarity assumption in statistically downscaled climate projections: is past performance an indicator of future results?. *Climatic Change*, *135*, 395-408.



Accepted for publication in *Journal of Applied Meteorology and Climatology*. DOI 10.1175/JAMC-D-23-0145.1.

Doblas-Reyes, F.J., A.A. Sörensson, M. Almazroui, A. Dosio, W.J. Gutowski, R. Haarsma, R. Hamdi, B. Hewitson, W.-T. Kwon, B.L. Lamptey, D. Maraun, T.S. Stephenson, I. Takayabu, L. Terray, A. Turner, and Z. Zuo, 2021: Linking Global to Regional Climate Change. In Climate Change 2021: The Physical Science Basis. Contribution of Working Group I to the Sixth Assessment Report of the Intergovernmental Panel on Climate Change [Masson-Delmotte, V., P. Zhai, A. Pirani, S.L. Connors, C. Péan, S. Berger, N. Caud, Y. Chen, L. Goldfarb, M.I. Gomis, M. Huang, K. Leitzell, E. Lonnoy, J.B.R. Matthews, T.K. Maycock, T. Waterfield, O. Yelekçi, R. Yu, and B. Zhou (eds.)]. Cambridge University Press, Cambridge, United Kingdom and New York, NY, USA, pp. 1363–1512, doi: 10.1017/9781009157896.012.

Domeisen, D. I., Eltahir, E. A., Fischer, E. M., Knutti, R., Perkins-Kirkpatrick, S. E., Schär, C., ... & Wernli, H. (2023). Prediction and projection of heatwaves. *Nature Reviews Earth & Environment*, *4*(1), 36-50.

Duchêne, F., Hamdi, R., Van Schaeybroeck, B., Caluwaerts, S., De Troch, R., De Cruz, L., & Termonia, P. (2022). Downscaling ensemble climate projections to urban scale: Brussels's future climate at 1.5° C, 2° C, and 3° C global warming. Urban Climate, 46, 101319.

Duchêne, F., Van Schaeybroeck, B., Caluwaerts, S., De Troch, R., Hamdi, R., & Termonia, P. (2020). A Statistical–dynamical methodology to downscale regional climate projections to urban scale. Journal of Applied Meteorology and Climatology, 59(6), 1109-1123.

Ekström, M., Grose, M. R., & Whetton, P. H. (2015). An appraisal of downscaling methods used in climate change research. Wiley Interdisciplinary Reviews: Climate Change, 6(3), 301-319.

Endlicher, W., Jendritzky, G., Fischer, J., & Redlich, J. P. (2008). Heat waves, urban climate and human health (pp. 269-278). Springer US.

Erbs, D. G., Klein, S. A., & Duffie, J. A. (1982). Estimation of the diffuse radiation fraction for hourly, daily and monthly-average global radiation. *Solar energy*, *28*(4), 293-302.

Eyring, V., Gillett, N. P., Achutarao, K., Barimalala, R., Barreiro Parrillo, M., Bellouin, N., ... & Sun, Y. (2021). Human Influence on the Climate System. In Climate Change 2021: The Physical Science Basis. Contribution of Working Group I to the Sixth Assessment



Accepted for publication in *Journal of Applied Meteorology and Climatology*. DOI 10.1175/JAMC-D-23-0145.1.

Report of the Intergovernmental Panel on Climate Change. *IPCC Sixth Assessment Report*.

Faroux, S., Kaptué Tchuenté, A. T., Roujean, J. L., Masson, V., Martin, E., & Le Moigne, P. (2013). ECOCLIMAP-II/Europe: A twofold database of ecosystems and surface parameters at 1 km resolution based on satellite information for use in land surface, meteorological and climate models. *Geoscientific Model Development*, *6*(2), 563-582.

Fischer, E. M., Oleson, K. W., & Lawrence, D. M. (2012). Contrasting urban and rural heat stress responses to climate change. Geophysical research letters, 39(3).

Frey-Buness, F., Heimann, D., & Sausen, R. (1995). A statistical-dynamical downscaling procedure for global climate simulations. Theoretical and Applied Climatology, 50, 117-131.

Früh, B., Becker, P., Deutschländer, T., Hessel, J. D., Kossmann, M., Mieskes, I., ... & Wienert, U. (2011). Estimation of climate-change impacts on the urban heat load using an urban climate model and regional climate projections. Journal of Applied Meteorology and Climatology, 50(1), 167-184.

Fuentes, U., & Heimann, D. (2000). An improved statistical-dynamical downscaling scheme and its application to the Alpine precipitation climatology. Theoretical and Applied Climatology, 65, 119-135.

Giorgi, F., & Gutowski Jr, W. J. (2015). Regional dynamical downscaling and the CORDEX initiative. Annual review of environment and resources, 40, 467-490.

Giorgi, F., Hewitson, B., Arritt, R., Gutowski, W., Gutowski, W., Knutson, T., & Landsea, C. (2001). Regional climate information—evaluation and projections.

Grimmond, C. S. B., Blackett, M., Best, M. J., Barlow, J., Baik, J. J., Belcher, S. E., ... & Zhang, N. (2010). The international urban energy balance models comparison project: first results from phase 1. Journal of applied meteorology and climatology, 49(6), 1268-1292.

Gutiérrez, C., Somot, S., Nabat, P., Mallet, M., Corre, L., Van Meijgaard, E., ... & Gaertner, M. Á. (2020). Future evolution of surface solar radiation and photovoltaic potential in Europe: investigating the role of aerosols. *Environmental Research Letters*, *15*(3), 034035.



Accepted for publication in *Journal of Applied Meteorology and Climatology*. DOI 10.1175/JAMC-D-23-0145.1.

Haeffelin, M., Barthès, L., Bock, O., Boitel, C., Bony, S., Bouniol, D., ... & Vautard, R. (2005, February). SIRTA, a ground-based atmospheric observatory for cloud and aerosol research. In *Annales Geophysicae* (Vol. 23, No. 2, pp. 253-275). Copernicus GmbH.

Hamdi, R., & Masson, V. (2008). Inclusion of a drag approach in the Town Energy Balance (TEB) scheme: Offline 1D evaluation in a street canyon. *Journal of Applied Meteorology and Climatology*, *47*(10), 2627-26

Hamdi, R., Giot, O., De Troch, R., Deckmyn, A., & Termonia, P. (**2015**). Future climate of Brussels and Paris for the 2050s under the A1B scenario. *Urban climate*, *12*, 160-182. https://doi.org/10.1016/j.uclim.2015.03.003

Hamdi, R., Van de Vyver, H., De Troch, R., & Termonia, P. (**2014**). Assessment of three dynamical urban climate downscaling methods: Brussels's future urban heat island under an A1B emission scenario. *International Journal of Climatology*, *34*(4), 978-999. https://doi.org/10.1002/joc.3734

Hatchett, B. J., Koračin, D., Mejía, J. F., & Boyle, D. P. (2016). Assimilating urban heat island effects into climate projections. Journal of Arid Environments, 128, 59-64.

Heaviside, C., Macintyre, H., & Vardoulakis, S. (2017). The urban heat island: implications for health in a changing environment. *Current environmental health reports*, *4*(3), 296-305.

Heaviside, C., Vardoulakis, S., & Cai, X. M. (2016). Attribution of mortality to the urban heat island during heatwaves in the West Midlands, UK. *Environmental health*, *15*(1), 49-59.

Hidalgo, J., & Jougla, R. (2018). On the use of local weather types classification to improve climate understanding: An application on the urban climate of Toulouse. *PloS one*, *13*(12), e0208138.

Hidalgo, J., Masson, V., & Baehr, C. (2014). From daily climatic scenarios to hourly atmospheric forcing fields to force Soil-Vegetation-Atmosphere transfer models. *Frontiers in Environmental Science*, *2*, 40.

Hoffmann, P., Schoetter, R., & Schlünzen, H. (2018). Statistical-dynamical downscaling of the urban heat island in Hamburg, Germany. Meteorologische Zeitschrift, 27, 89-109.



Accepted for publication in *Journal of Applied Meteorology and Climatology*. DOI 10.1175/JAMC-D-23-0145.1.

Hyndman, R. J., & Fan, Y. (1996). Sample quantiles in statistical packages. The American Statistician, 50(4), 361-365.

Jacob, D., Petersen, J., Eggert, B., Alias, A., Christensen, O. B., Bouwer, L. M., ... & Yiou, P. (2014). EURO-CORDEX: new high-resolution climate change projections for European impact research. *Regional environmental change*, *14*(2), 563-578.

Jacob, D., Teichmann, C., Sobolowski, S., Katragkou, E., Anders, I., Belda, M., ... & Wulfmeyer, V. (2020). Regional climate downscaling over Europe: perspectives from the EURO-CORDEX community. *Regional environmental change*, *20*(2), 1-20.

Jennings, K. S., Winchell, T. S., Livneh, B., & Molotch, N. P. (2018). Spatial variation of the rain–snow temperature threshold across the Northern Hemisphere. *Nature communications*, *9*(1), 1-9.

Jougla, R., Hidalgo, J., & Pouponneau, B. (2019). Identification des situations météorologiques locales pour une cinquantaine de villes françaises. *La Météorologie*, *2019*(106), 59-68.

Keat, W. J., Kendon, E. J., & Bohnenstengel, S. I. (2021). Climate change over UK cities: the urban influence on extreme temperatures in the UK climate projections. Climate Dynamics, 57(11), 3583-3597.

Keppas, S. C., Papadogiannaki, S., Parliari, D., Kontos, S., Poupkou, A., Tzoumaka, P., ... & Melas, D. (2021). Future climate change impact on urban heat island in two mediterranean cities based on high-resolution regional climate simulations. *Atmosphere*, *12*(7), 884.

Kotlarski, S., Keuler, K., Christensen, O. B., Colette, A., Déqué, M., Gobiet, A., ... & Wulfmeyer, V. (2014). Regional climate modeling on European scales: a joint standard evaluation of the EURO-CORDEX RCM ensemble. Geoscientific Model Development, 7(4), 1297-1333.

Kounkou-Arnaud, R., & Brion, D. (2018, August). Optimal interpolation of daily temperatures around Paris, taking into account urban fraction. In International Conference of Urban Climate ICUC (Vol. 10).

Krakauer, N. Y., & Devineni, N. (2015). Up-to-date probabilistic temperature climatologies. *Environmental Research Letters*, *10*(2), 024014.





Accepted for publication in *Journal of Applied Meteorology and Climatology*. DOI 10.1175/JAMC-D-23-0145.1.

Kwok, Y. T., Schoetter, R., Lau, K. K. L., Hidalgo, J., Ren, C., Pigeon, G., & Masson, V. (2019). How well does the local climate zone scheme discern the thermal environment of Toulouse (France)? An analysis using numerical simulation data. *International Journal of Climatology*, *39*(14), 5292-5315.

Lac, C., Chaboureau, J. P., Masson, V., Pinty, J. P., Tulet, P., Escobar, J., ... & Wautelet, P. (2018). Overview of the Meso-NH model version 5.4 and its applications. *Geoscientific Model Development*, *11*(5), 1929-1969.

Lafore, J. P., Stein, J., Asencio, N., Bougeault, P., Ducrocq, V., Duron, J., ... & Vilà-Guerau de Arellano, J. (1998). The Meso-NH atmospheric simulation system. Part I: Adiabatic formulation and control simulations. In *Annales geophysicae* (Vol. 16, No. 1, pp. 90-109). Göttingen, Germany: Springer Verlag.

Langendijk, G. S., Rechid, D., & Jacob, D. (2019). Urban areas and urban–rural contrasts under climate change: what does the EURO-CORDEX ensemble tell us?—Investigating near surface humidity in Berlin and its surroundings. *Atmosphere*, *10*(12), 730.

Lauwaet, D., De Ridder, K., Saeed, S., Brisson, E., Chatterjee, F., Van Lipzig, N. P. M., ... & Hooyberghs, H. (2015a). Assessing the current and future urban heat island of Brussels. Urban Climate, 15, 1-15.

Lauwaet, D., Hooyberghs, H., Maiheu, B., Lefebvre, W., Driesen, G., Van Looy, S., & De Ridder, K. (2015b). Detailed urban heat island projections for cities worldwide: dynamical downscaling CMIP5 global climate models. Climate, 3(2), 391-415.

Le Roy, B., Lemonsu, A., & Schoetter, R. (2021). A statistical–dynamical downscaling methodology for the urban heat island applied to the EURO-CORDEX ensemble. *Climate Dynamics*, *56*(7), 2487-2508.

Le Roy, B., Lemonsu, A., Kounkou-Arnaud, R., Brion, D., & Masson, V. (2020). Long time series spatialized data for urban climatological studies: A case study of Paris, France. *International Journal of Climatology*, *40*(7), 3567-3584.

Lee, J.-Y., J. Marotzke, G. Bala, L. Cao, S. Corti, J.P. Dunne, F. Engelbrecht, E. Fischer, J.C. Fyfe, C. Jones, A. Maycock, J. Mutemi, O. Ndiaye, S. Panickal, and T. Zhou, 2021: Future Global Climate: Scenario-Based Projections and Near-Term Information. In Climate Change 2021: The Physical Science Basis. Contribution of Working Group I to the Sixth Assessment Report of the Intergovernmental Panel on Climate Change



Accepted for publication in *Journal of Applied Meteorology and Climatology*. DOI 10.1175/JAMC-D-23-0145.1.

[Masson-Delmotte, V., P. Zhai, A. Pirani, S.L. Connors, C. Péan, S. Berger, N. Caud, Y. Chen, L. Goldfarb, M.I. Gomis, M. Huang, K. Leitzell, E. Lonnoy, J.B.R. Matthews, T.K. Maycock, T. Waterfield, O. Yelekçi, R. Yu, and B. Zhou (eds.)]. Cambridge University Press, Cambridge, United Kingdom and New York, NY, USA, pp. 553–672, doi: 10.1017/9781009157896.006.

Lemonsu, A., Caillaud, C., Alias, A., Riette, S., Seity, Y., Le Roy, B., ... & Lucas-Picher, P. (2023). What added value of CNRM-AROME convection-permitting regional climate model compared to CNRM-ALADIN regional climate model for urban climate studies? Evaluation over Paris area (France). *Climate Dynamics*, 1-19.

Lemonsu, A., Kounkou-Arnaud, R., Desplat, J., Salagnac, J. L., & Masson, V. (2013). Evolution of the Parisian urban climate under a global changing climate. *Climatic change*, *116*(3), 679-692.

Lemonsu, A., Masson, V., Shashua-Bar, L., Erell, E., & Pearlmutter, D. (2012). Inclusion of vegetation in the Town Energy Balance model for modelling urban green areas. *Geoscientific Model Development*, *5*(6), 1377-1393.

Lemonsu, A., Munck, C. D., Kounkou-Arnaud, R., Masson, V., & Viguié, V. (2021). What Alternatives Does Paris Have to Adapt to Future Heat Waves?. In *Urban Climate Science for Planning Healthy Cities* (pp. 239-258). Springer, Cham.

Lemonsu, A., Viguie, V., Daniel, M., & Masson, V. (2015). Vulnerability to heat waves: Impact of urban expansion scenarios on urban heat island and heat stress in Paris (France). *Urban Climate*, *14*, 586-605.

Leung, D. Y. (2015). Outdoor-indoor air pollution in urban environment: challenges and opportunity. Frontiers in Environmental Science, 2, 69.

Lind, P., Belušić, D., Médus, E., Dobler, A., Pedersen, R. A., Wang, F., ... & Christensen, J. H. (2022). Climate change information over Fenno-Scandinavia produced with a convection-permitting climate model. Climate Dynamics, 1-23.

Lindvall, J., & Svensson, G. (2015). The diurnal temperature range in the CMIP5 models. *Climate Dynamics*, *44*, 405-421.



Accepted for publication in *Journal of Applied Meteorology and Climatology*. DOI 10.1175/JAMC-D-23-0145.1.

Lo, Y. E., Mitchell, D. M., Bohnenstengel, S. I., Collins, M., Hawkins, E., Hegerl, G. C., ... & Stott, P. A. (2020). UK climate projections: Summer daytime and nighttime urban heat island changes in England's major cities. Journal of Climate, 33(20), 9015-9030.

Luber, G., & McGeehin, M. (2008). Climate change and extreme heat events. American journal of preventive medicine, 35(5), 429-435.

Lucas-Picher, P., Argüeso, D., Brisson, E., Tramblay, Y., Berg, P., Lemonsu, A., ... & Caillaud, C. (2021). Convection-permitting modeling with regional climate models: Latest developments and next steps. Wiley Interdisciplinary Reviews: Climate Change, 12(6), e731.

Mann, H. B., & Whitney, D. R. (1947). On a test of whether one of two random variables is stochastically larger than the other. *The annals of mathematical statistics*, 50-60.

Masson-Delmotte, V., Zhai, P., Pirani, A., Connors, S. L., Péan, C., Berger, S., ... & Zhou, B. (2021). Climate change 2021: the physical science basis. *Contribution of working group I to the sixth assessment report of the intergovernmental panel on climate change*, *2*.

Masson, V. (2000). A physically-based scheme for the urban energy budget in atmospheric models. *Boundary-layer meteorology*, *94*(3), 357-397.

Masson, V. (2006). Urban surface modeling and the meso-scale impact of cities. Theoretical and applied climatology, 84, 35-45.

Masson, V., Le Moigne, P., Martin, E., Faroux, S., Alias, A., Alkama, R., ... & Voldoire, A. (2013). The SURFEXv7. 2 land and ocean surface platform for coupled or offline simulation of earth surface variables and fluxes. *Geoscientific Model Development*, *6*(4), 929-960.

McCarthy, M. P., Best, M. J., & Betts, R. A. (2010). Climate change in cities due to global warming and urban effects. Geophysical research letters, 37(9).

McCarthy, M. P., Harpham, C., Goodess, C. M., & Jones, P. D. (2012). Simulating climate change in UK cities using a regional climate model, HadRM3. International Journal of Climatology, 32(12), 1875-1888.

McMichael, A. J., Woodruff, R. E., & Hales, S. (2006). Climate change and human health: present and future risks. The Lancet, 367(9513), 859-869.



Accepted for publication in *Journal of Applied Meteorology and Climatology*. DOI 10.1175/JAMC-D-23-0145.1.

Mengelkamp, H. T., Kapitza, H., & Pflueger, U. (1997). Statistical-dynamical downscaling of wind climatologies. Journal of Wind Engineering and Industrial Aerodynamics, 67, 449-457.

Mezghani, A., Dobler, A., Benestad, R., Haugen, J. E., Parding, K. M., Piniewski, M., & Kundzewicz, Z. W. (2019). Subsampling impact on the climate change signal over Poland based on simulations from statistical and dynamical downscaling. *Journal of Applied Meteorology and Climatology*, *58*(5), 1061-1078.

Nogueira, M., Lima, D. C., & Soares, P. M. (**2020**). An integrated approach to project the future urban climate response: Changes to Lisbon's urban heat island and temperature extremes. *Urban Climate*, *34*, 100683. https://doi.org/10.1016/j.uclim.2020.100683

Noilhan, J., & Mahfouf, J. F. (1996). The ISBA land surface parameterisation scheme. *Global and planetary Change*, *13*(1-4), 145-159.

Noilhan, J., & Planton, S. (1989). A simple parameterization of land surface processes for meteorological models. *Monthly weather review*, *117*(3), 536-549.

Nunez, M., & Oke, T. R. (1977). The energy balance of an urban canyon. *Journal of Applied Meteorology and Climatology*, *16*(1), 11-19.

Oke, T. R. (1984). Methods in urban climatology. Applied Climatology, 14(18), 19-29.

Oke, T. R. (1988). The urban energy balance. *Progress in Physical geography*, *12*(4), 471-508.

Oke, T. R., Mills, G., Christen, A., & Voogt, J. A. (2017). Urban climates. Cambridge University Press.

Oleson, K. (2012). Contrasts between urban and rural climate in CCSM4 CMIP5 climate change scenarios. Journal of Climate, 25(5), 1390-1412.

Oleson, K. W., Bonan, G. B., Feddema, J., & Jackson, T. (2011). An examination of urban heat island characteristics in a global climate model. International Journal of Climatology, 31(12), 1848-1865.

Ozturk, T., Matte, D., & Christensen, J. H. (2021). Robustness of future atmospheric circulation changes over the EURO-CORDEX domain. *Climate Dynamics*, 1-16.

Pigeon, G., Zibouche, K., Bueno, B., Le Bras, J., & Masson, V. (2014). Improving the capabilities of the Town Energy Balance model with up-to-date building energy



Accepted for publication in *Journal of Applied Meteorology and Climatology*. DOI 10.1175/JAMC-D-23-0145.1.

simulation algorithms: an application to a set of representative buildings in Paris. *Energy and buildings*, *76*, 1-14.

Prein, A. F., Gobiet, A., Truhetz, H., Keuler, K., Goergen, K., Teichmann, C., ... & Jacob, D. (2016). Precipitation in the EURO-CORDEX 0.11^∘ 0. 11∘ and 0.44^∘ 0. 44∘ simulations: high resolution, high benefits?. *Climate dynamics*, *46*, 383-412.

R Core Team (2022). R: A language and environment for statistical computing. R Foundation for Statistical Computing, Vienna, Austria. https://www.R-project.org/

Redon, E. C., Lemonsu, A., Masson, V., Morille, B., & Musy, M. (2017). Implementation of street trees within the solar radiative exchange parameterization of TEB in SURFEX v8. 0. *Geoscientific Model Development*, *10*(1), 385-411.

Redon, E., Lemonsu, A., & Masson, V. (2020). An urban trees parameterization for modeling microclimatic variables and thermal comfort conditions at street level with the Town Energy Balance model (TEB-SURFEX v8. 0). *Geoscientific Model Development*, *13*(2), 385-399.

Riahi, K., Rao, S., Krey, V., Cho, C., Chirkov, V., Fischer, G., ... & Rafaj, P. (2011). RCP 8.5—A scenario of comparatively high greenhouse gas emissions. *Climatic change*, *109*(1), 33-57.

Ribes, A., Boé, J., Qasmi, S., Dubuisson, B., Douville, H., & Terray, L. (2022). An updated assessment of past and future warming over France based on a regional observational constraint. *Earth System Dynamics Discussions*, 1-29.

Rigal, A., Azaïs, J. M., & Ribes, A. (2019). Estimating daily climatological normals in a changing climate. *Climate dynamics*, *53*, 275-286.

Rizwan, A. M., Dennis, L. Y., & Chunho, L. I. U. (2008). A review on the generation, determination and mitigation of Urban Heat Island. Journal of environmental sciences, 20(1), 120-128.

Røste, J., & Landgren, O. A. (2022). Impacts of dynamical downscaling on circulation type statistics in the Euro-CORDEX ensemble. *Climate Dynamics*, 1-22.

Rummukainen, M. (2010). State-of-the-art with regional climate models. Wiley Interdisciplinary Reviews: Climate Change, 1(1), 82-96.

Rummukainen, M. (2016). Added value in regional climate modeling. *Wiley Interdisciplinary Reviews: Climate Change*, *7*(1), 145-159.

Sachindra, D. A., Ng, A. W. M., Muthukumaran, S., & Perera, B. J. C. (2016). Impact of climate change on urban heat island effect and extreme temperatures: a case-study. Quarterly Journal of the Royal Meteorological Society, 142(694), 172-186.

Salvi, K., Ghosh, S., & Ganguly, A. R. (2016). Credibility of statistical downscaling under nonstationary climate. Climate Dynamics, 46, 1991-2023.

Santamouris, M. (2020). Recent progress on urban overheating and heat island research. Integrated assessment of the energy, environmental, vulnerability and health impact. Synergies with the global climate change. *Energy and Buildings*, *207*, 109482.

Scherrer, S. C., Appenzeller, C., & Liniger, M. A. (2006). Temperature trends in Switzerland and Europe: implications for climate normals. *International Journal of Climatology: A Journal of the Royal Meteorological Society*, *26*(5), 565-580.

Schoetter, R., Hidalgo, J., Jougla, R., Masson, V., Rega, M., & Pergaud, J. (2020). A Statistical–Dynamical Downscaling for the Urban Heat Island and Building Energy Consumption—Analysis of Its Uncertainties. *Journal of Applied Meteorology and Climatology*, *59*(5), 859-883.

Schoetter, R., Masson, V., Bourgeois, A., Pellegrino, M., & Lévy, J. P. (2017). Parametrisation of the variety of human behaviour related to building energy consumption in the Town Energy Balance (SURFEX-TEB v. 8.2). *Geoscientific Model Development*, *10*(7), 2801-2831.

Schoof, J. T. (2013). Statistical downscaling in climatology. Geography Compass, 7(4), 249-265.

Schwingshackl, C., Davin, E. L., Hirschi, M., Sørland, S. L., Wartenburger, R., & Seneviratne, S. I. (2019). Regional climate model projections underestimate future warming due to missing plant physiological CO2 response. *Environmental Research Letters*, *14*(11), 114019.

Sedlar, J., & Hock, R. (2009). Testing longwave radiation parameterizations under clear and overcast skies at Storglaciären, Sweden. *The Cryosphere*, *3*(1), 75-84.



Accepted for publication in *Journal of Applied Meteorology and Climatology*. DOI 10.1175/JAMC-D-23-0145.1.

Seneviratne, S.I., X. Zhang, M. Adnan, W. Badi, C. Dereczynski, A. Di Luca, S. Ghosh, I. Iskandar, J. Kossin, S. Lewis, F. Otto, I. Pinto, M. Satoh, S.M. Vicente-Serrano, M. Wehner, and B. Zhou, 2021: Weather and Climate Extreme Events in a Changing Climate. In Climate Change 2021: The Physical Science Basis. Contribution of Working Group I to the Sixth Assessment Report of the Intergovernmental Panel on Climate Change[Masson-Delmotte, V., P. Zhai, A. Pirani, S.L. Connors, C. Péan, S. Berger, N. Caud, Y. Chen, L. Goldfarb, M.I. Gomis, M. Huang, K. Leitzell, E. Lonnoy, J.B.R. Matthews, T.K. Maycock, T. Waterfield, O. Yelekçi, R. Yu, and B. Zhou (eds.)]. Cambridge University Press, Cambridge, United Kingdom and New York, NY, USA, pp. 1513–1766, doi: 10.1017/9781009157896.013.

Sharma, R., Hooyberghs, H., Lauwaet, D., & De Ridder, K. (2019). Urban heat island and future climate change—Implications for Delhi's heat. Journal of Urban Health, 96(2), 235-251.

Solman, S. A., & Blázquez, J. (2019). Multiscale precipitation variability over South America: analysis of the added value of CORDEX RCM simulations. *Climate Dynamics*, *53*(3), 1547-1565.

Sørland, S. L., Schär, C., Lüthi, D., & Kjellström, E. (2018). Bias patterns and climate change signals in GCM-RCM model chains. *Environmental Research Letters*, *13*(7), 074017.

Spinoni, J., Vogt, J. V., Naumann, G., Barbosa, P., & Dosio, A. (2018). Will drought events become more frequent and severe in Europe?. International Journal of Climatology, 38(4), 1718-1736.

Stewart, I. D. (2011). A systematic review and scientific critique of methodology in modern urban heat island literature. International Journal of Climatology, 31(2), 200-217.

Tabary, P., Dupuy, P., L'Henaff, G., Gueguen, C., Moulin, L., & Laurantin, O. (2012). A 10-year (1997—2006) reanalysis of Quantitative Precipitation Estimation over France: methodology and first results. *IAHS-AISH publication*, (351), 255-260.

Tan, J., Zheng, Y., Tang, X., Guo, C., Li, L., Song, G., ... & Chen, H. (2010). The urban heat island and its impact on heat waves and human health in Shanghai. *International journal of biometeorology*, *54*(1), 75-84.

Tapiador, F. J., Navarro, A., Moreno, R., Sánchez, J. L., & García-Ortega, E. (2020). Regional climate models: 30 years of dynamical downscaling. Atmospheric Research, 235, 104785.

Taylor, K. E., Stouffer, R. J., & Meehl, G. A. (2012). An overview of CMIP5 and the experiment design. *Bulletin of the American meteorological Society*, *93*(4), 485-498.

Thomson, A. M., Calvin, K. V., Smith, S. J., Kyle, G. P., Volke, A., Patel, P., ... & Edmonds, J. A. (2011). RCP4. 5: a pathway for stabilization of radiative forcing by 2100. *Climatic change*, *109*(1), 77-94.

Trusilova, K., Früh, B., Brienen, S., Walter, A., Masson, V., Pigeon, G., & Becker, P. (2013). Implementation of an urban parameterization scheme into the regional climate model COSMO-CLM. Journal of Applied Meteorology and Climatology, 52(10), 2296-2311.

Tyler, S., & Moench, M. (2012). A framework for urban climate resilience. Climate and development, 4(4), 311-326.

Unsworth, M. H., & Monteith, J. L. (1975). Long-wave radiation at the ground I. Angular distribution of incoming radiation. *Quarterly Journal of the Royal Meteorological Society*, *101*(427), 13-24.

Van Vuuren, D. P., Edmonds, J., Kainuma, M., Riahi, K., Thomson, A., Hibbard, K., ... & Rose, S. K. (2011). The representative concentration pathways: an overview. *Climatic change*, *109*(1), 5-31.

Vautard, R., Kadygrov, N., Iles, C., Boberg, F., Buonomo, E., Bülow, K., ... & Wulfmeyer, V. (2021). Evaluation of the large EURO-CORDEX regional climate model ensemble. *Journal of Geophysical Research: Atmospheres*, *126*(17), e2019JD032344.

Viguié, V., Hallegatte, S., & Rozenberg, J. (2014). Downscaling long term socio-economic scenarios at city scale: A case study on Paris. *Technological forecasting and social change*, *87*, 305-324.

Wilby RL (2007) A review of climate change impacts on the built environment. Built Environ 33(1):31–45. https://doi.org/10.2148/benv.33.1.31

Wilby, R. L., & Wigley, T. M. (1997). Downscaling general circulation model output: a review of methods and limitations. Progress in physical geography, 21(4), 530-548.

Wilby, R. L., Charles, S. P., Zorita, E., Timbal, B., Whetton, P., & Mearns, L. O. (2004). Guidelines for use of climate scenarios developed from statistical downscaling methods. Supporting material of the Intergovernmental Panel on Climate Change, available from the DDC of IPCC TGCIA, 27.

Wilcoxon, F. (1945). Individual comparisons by ranking methods. Biom. Bull., 1, 80–83.

Wong, L. P., Alias, H., Aghamohammadi, N., Aghazadeh, S., & Sulaiman, N. M. N. (2017). Urban heat island experience, control measures and health impact: A survey among working community in the city of Kuala Lumpur. *Sustainable cities and society*, *35*, 660-668.

Xu, Z., Han, Y., & Yang, Z. (2019). Dynamical downscaling of regional climate: A review of methods and limitations. Science China Earth Sciences, 62, 365-375.

Zhao, L., Oppenheimer, M., Zhu, Q., Baldwin, J. W., Ebi, K. L., Bou-Zeid, E., ... & Liu, X. (2018). Interactions between urban heat islands and heat waves. *Environmental research letters*, *13*(3), 034003.

Žuvela-Aloise, M., Koch, R., Buchholz, S., & Früh, B. (2016). Modelling the potential of green and blue infrastructure to reduce urban heat load in the city of Vienna. Climatic Change, 135, 425-438.



Accepted for publication in *Journal of Applied Meteorology and Climatology*. DOI 10.1175/JAMC-D-23-0145.1.

SUPPLEMENTAL MATERIALS LE ROY ET AL. 2024

Table S1. List of the Global Climate Models that were downscaled by the EURO–CORDEX ensemble used in the present study.

| Modeling Center | Global Climate Model | Reference |
|---|---|---|
| CNRM–CERFACS | CNRM–CM5 | Voldoire et al. (2013) |
| ICHEC | EC–EARTH | Hazeleger et al. (2010; 2012) |
| IPSL | IPSL–CM5–MR | Dufresne et al. (2013) |
| MOHC | HadGEM2–ES | Collins et al. (2011) |
| MPI–M | MPI–ESM–LR | Giorgetta et al. (2013) |
| NCC | NorESM1–M | Bentsen et al. (2013) and Iversen et al. (2013) |

Table S2. List of the Regional Climate Models from the EURO–CORDEX ensemble used in the present study.

| Modeling Center | Regional Climate Model | Reference |
|---|---|---|
| CNRM | ALADIN63 | Daniel et al. (2019) |
| CLMcom–ETH | COSMO–crCLIM–v1–1 | Sørland et al. (2021) |
| DMI | HIRHAM5 | Christensen et al. (2007) |
| MOHC | HadREM3–GA7–05 | – |
| KNMI | RACMO22E | van Meijgaard et al. (2008; 2012) |
| SMHI | RCA4 | Samuelsson et al. (2015) |
| ICTP | RegCM4–6 | Giorgi et al. (2012) |
| GERICS | REMO2015 | Jacob et al. (2012) |

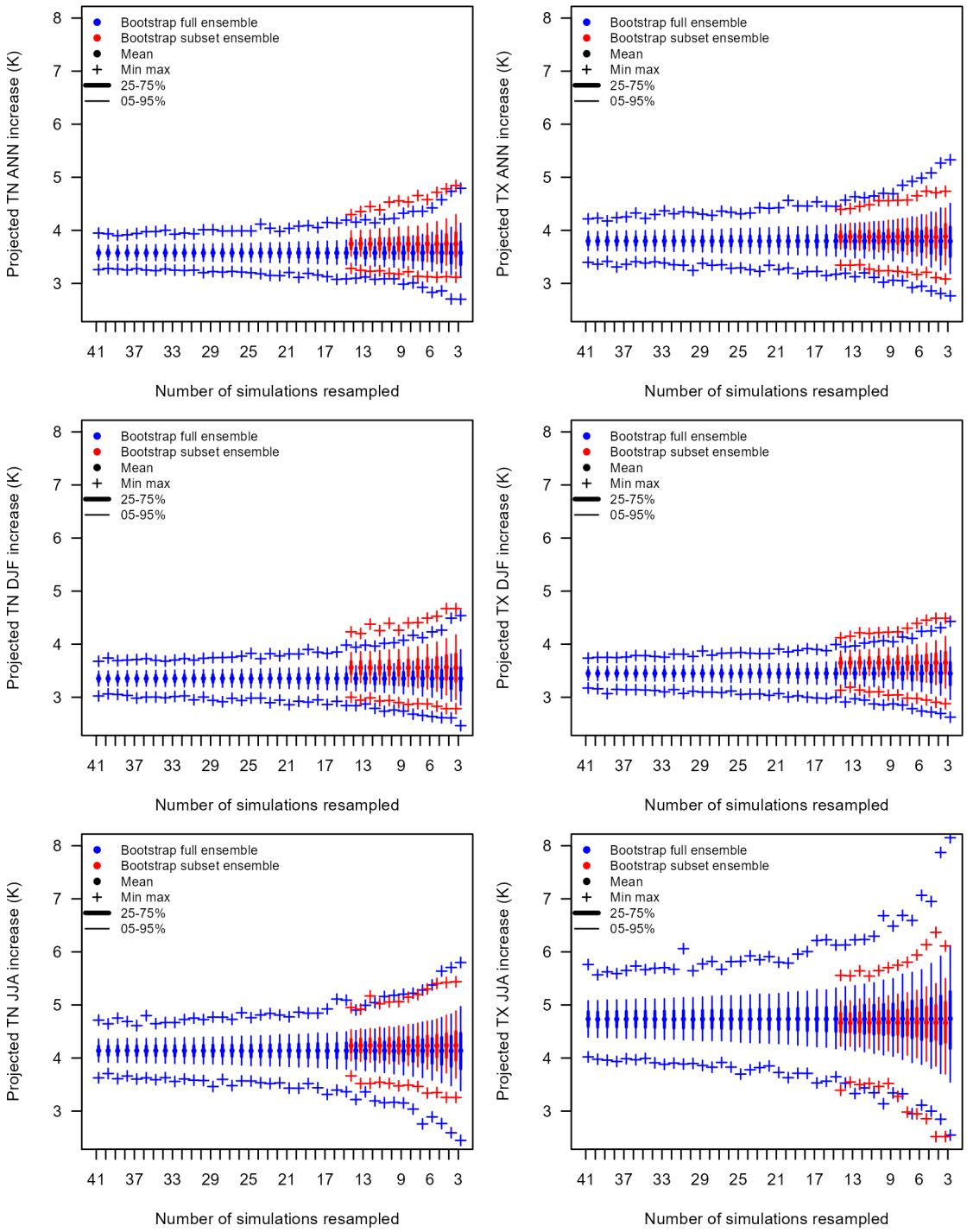


Fig. S1 Average warming statistics obtained by resampling 10,000 times n simulations from the full ensemble of 41 simulations (blue) and the subset of 14 simulations (red). Warming is computed between 2080–2099 and 1976–2005 under scenario RCP8.5 for TN and TX and for ANN, DJF and JJA. Following the boostrap resampling approach of Mezghani et al. (2019).

## A. Correction of Regional Climate Model outputs

Given that one of the goal of the downscaling framework is to be able to produce impacts indicators related to air temperature such as energy consumption of buildings or thermal comfort of inhabitants, the RCMs need to be corrected. The choice is made to apply a simple correction scheme that changes the occurrence frequencies of LWTs simulated by the RCMs as little as possible. Given that the LWTs are defined using daily thermal amplitude (dT) we therefore correct the daily average temperature (TM) as to not change dT. Monthly averages of TM are computed over the period 1976–2005 (12 values) for each RCM and compared to the one obtained using the AURELHY spatialized observation dataset. AURELHY points are selected in the same way as EURO–CORDEX ones: as the average of a ring between 30 and 60 km on each dataset native grid. Monthly TM biases are then computed and used to correct (1) daily TN and TX over the whole period 1970–2099 and (2) 3–hourly air temperature based on the month.

Two other variables related to air temperature are also corrected. Longwave radiation is modified according to the corrected air temperature and to keep the original emissivity of the RCM ($LW_{cor} = \varepsilon_{ori}\sigma T_{cor}^4$). Likewise, the specific humidity is corrected to keep the relative humidity simulated by the RCM. Now, since the daily average specific humidity is also used to define the LWTs it is also modified, which has only a slight impact on the occurrence frequencies of LWTs.

Note that the daily average specific humidity of a day might be different than the average of the 3–hourly values of the same day depending if it is a diagnostic directly computed by the model or post processed afterwards. To take that into account we compute the ratio of daily average specific humidity to average of 3–hourly specific humidity for each day and use it to find the corrected value.

## B. Adaptation of the statistical–dynamical downscaling for the production of atmospheric forcings

Le Roy et al. (2021a) developed a statistical–dynamical downscaling (SDD) approach to reconstruct 2–meters Urban Heat Island (UHI) maps over the period 2000–2009. Here the method has been extended to produce atmospheric forcings that can then be used to drive the Land Surface Model SURFEX (Table S3).

Table S3. Description of the climate data required for the SURFEX forcing and the downscaling reconstruction. RCM denotes the values provided by the RCM, Meso–NH the spatialized fields calculated from the high–resolution simulations, and SPA the spatialized field combining RCM and Meso–NH. Adapted from Le Roy (2021b).

| **Variable** | **Unit** | **Source** | **Resolution** |
|---|---|---|---|
| Air temperature | (K) | $f$ ($T_{RCM}$, $T_{Meso–NH}$) | 1 km |
| Atmospheric pressure | (Pa) | $f$ ($PS_{RCM}$, $PS_{Meso–NH}$) | 1 km |
| Longwave radiation | (W.m–2) | $f$ ($LW_{RCM}$, $T_{SPA}$) | 1 km ($\varepsilon_{RCM}$* uniform) |
| Air specific humidity | (kg.kg–1) | $f$ ($U_{RCM}$**, $T_{SPA}$, $PS_{SPA}$) | 1 km ($U_{RCM}$** uniform) |
| Liquid precipitation rate | (mm.s–1) | $f$ ($RR_{RCM}$, $T_{SPA}$) | 1 km ($RR_{RCM}$ uniform) |
| Solid precipitation rate | (mm.s–1) | $f$ ($RR_{RCM}$, $T_{SPA}$) | 1 km ($RR_{RCM}$ uniform) |
| Direct shortwave radiation | (W.m–2) | $SW_{RCM}$ | Uniform |
| Diffuse shortwave radiation | (W.m–2) | $SW_{RCM}$ | Uniform |
| Wind speed | (m.s–1) | $FF_{RCM}$ | Uniform |
| Wind direction | (°) | Constant | Uniform |

* $\varepsilon_{RCM}$ refers to the apparent emissivity of the air defined by $\epsilon_{RCM} = \frac{LW_{RCM}}{\sigma \times T_{RCM}^4}$, with σ = 5.670374419× $10^{-8}$ $W.m^{-2}.K^{-1}$.

** $U_{RCM}$ refers to the absolute humidity of the air.

*I. Attribution of a Local Weather Type and the associated urban footprint*

Daily variables are extracted from one Regional Climate Model of the EURO–CORDEX ensemble, corrected, and used to define the Local Weather Types (LWT) of each day, in the historical period as well as in the future. The necessary variables for the LWT attribution are: thermal daily amplitude, daily average specific humidity, precipitation, wind speed and direction.

A "Meso–NH day" (see Le Roy et al. 2021a) is associated to each day based on the LWT that was attributed. The urban footprint on air temperature at different heights (starting at 2 m) is available for every hour of each "Meso–NH day".

*II. Computation of missing variables*

Some variables required to drive SURFEX are not provided by the EURO–CORDEX ensemble: the separation of precipitation into snow and rain, and the separation of the downwelling shortwave radiation into direct and scattered.

Following Jennings et al. (2018) analyses of the rain–snow temperature threshold across the Northern Hemisphere we consider that if the air temperature is inferior to 1 K, the total precipitation is defined as rain and snow otherwise.

To separate the downwelling shortwave radiation we use the statistical model by Erbs et al. (1982).

*III. Correction of the height of the RCM outputs*

Three hourly variables are extracted and corrected from the EURO–CORDEX ensemble. They are located near the surface (2 m) and need to be corrected to the desired forcing height (50 meters in our case). First the wind speed is corrected using a logarithmic wind profile with a standard zero displacement height for vegetation. Then the height correction is done following the method developed by Lemonsu et al. (2012): SURFEX is forced a first time over a typical natural point using the 2 m outputs from the RCM but prescribed at the desired height (50 m). The difference between the SURFEX output (2 m air temperature) is then used to correct the original forcing (RCM); the simulation is carried out again with this time the

corrected RCM outputs. 3 iterations of simulations are enough for the temperature to converge. For the first iteration the original wind speed of the RCM is used, afterwards the corrected 50 m values are used. After each iteration the specific humidity is adjusted with the new air temperature to keep the original relative humidity of the RCM. The same thing is done for downwelling long–wave radiation to keep the apparent air emissivity of the RCM (Unsworth & Monteith, 1975; Sedlar & Hock 2009; Lauwaet et al. 2015).

*IV. Addition of the urban footprint to the RCM outputs*

We now have 50 m three–hourly variables with no urban effect. The urban footprint is added on air temperature, as well as atmospheric pressure, using the "Meso–NH day" hourly values of step 1. Given that the nighttime UHI is influenced by the atmospheric conditions of the previous day the correction is made from 9 UTC to 6 UTC the following day. Following what was done in step 3, humidity, long–wave radiation and snow and rain are spatialized using the new temperature incorporating the urban footprint. For the other variables (shortwave and wind speed) we simply apply the RCM values uniformly over the domain. We end up with 3–hourly 1–km horizontal resolution maps for the variables listed in Table S3.

Table S4. TN, TX and TM biases of the ensemble of 41 simulations (average and inter quartile range) before and after the correction of TM over the period 1976–2005.

| | **TN** | | **TX** | | **TM** |
|---|---|---|---|---|---|
| | Before TM correction | After TM correction | Before TM correction | After TM correction | Before TM correction |
| **DJF** | 0.5 [-0.1 – 1.2] | 0.3 [0.0 – 0.7] | -0.2 [-0.7 – 0.5] | -0.3 [-0.7 – -0.1] | 0.2 [-0.4 – 0.7] |
| **MAM** | 0.3 [-0.4 – 1.5] | 0.7 [0.5 – 1.0] | -1.1 [-2.1 – -0.3] | -0.7 [-1.0 – -0.5] | -0.4 [-1.0 – 0.6] |
| **JJA** | 0.7 [-0.3 – 1.4] | 1.0 [0.7 – 1.3] | -1.3 [-2.5 – -0.3] | -1.0 [-1.3 – -0.6] | -0.3 [-1.4 – 0.5] |
| **SON** | 0.4 [-0.4 – 1.2] | 0.7 [0.3 – 1.0] | -1.1 [-1.7 – -0.5] | -0.7 [-1.0 – -0.3] | -0.4 [-0.8 – 0.2] |

Table S5. As for Table 1 in main document: average temperatures and UHI intensities for all the summer days over the period 2000-2017, plus averages of the days with $UHI_N$ and $UHI_X$ above their respective 90$^{th}$ percentiles.

| | | Observation | Simulation (14) | Simulation (41) | Bias (14) | Bias (41) |
|---|---|---|---|---|---|---|
| All JJA days (2000-2017) | $TN_{URB}$ (°C) | 15.4 | 16.3 | 16.4 | +0.8 | +1.0 |
| | $TN_{RUR}$ (°C) | 12.7 | 14.2 | 14.2 | +1.5 | +1.6 |
| | $UHI_N$ (°C) | 2.8 | 2.1 | 2.2 | -0.7 | -0.6 |
| | $TX_{URB}$ (°C) | 24.8 | 24.1 | 24.0 | -0.7 | -0.8 |
| | $TX_{RUR}$ (°C) | 24.4 | 23.2 | 23.3 | -1.2 | -1.1 |
| | $UHI_X$ (°C) | 0.5 | 0.9 | 0.8 | +0.4 | +0.3 |
| JJA days with $UHI_N \geq P_{90}UHI_N$ | $TN_{URB}$ (°C) | 16.6 | 15.5 | 16.0 | -1.1 | -0.6 |
| | $TN_{RUR}$ (°C) | 11.3 | 12.2 | 12.4 | 0.8 | 1.1 |
| | $UHI_N$ (°C) | 5.2 | 3.4 | 3.6 | -1.8 | -1.6 |
| JJA days with $UHI_X \geq P_{90}UHI_X$ | $TX_{URB}$ (°C) | 26.1 | 23.8 | 23.3 | -2.3 | -2.8 |
| | $TX_{RUR}$ (°C) | 24.3 | 22.0 | 21.6 | -2.3 | -2.7 |
| | $UHI_X$ (°C) | 1.6 | 1.7 | 1.7 | +0.1 | +0.1 |

Table S6. Projected rural temperature change in the near and far future (2030–2049 and 2080–2099) in comparison to the historical period (1976–2005). In addition to the mean, the spread of the ensemble is represented by the percentiles 25 and 75.

| | | $TN_{RUR}$ | | $TX_{RUR}$ | |
|---|---|---|---|---|---|
| | | 2030–2049 | 2080–2099 | 2030–2049 | 2080–2099 |
| RCP4.5 (14) | ANN | 1.2 [1.0 – 1.2] | 1.9 [1.7 – 2.2] | 1.2 [1.0 – 1.3] | 2.0 [1.7 – 2.2] |
| | DJF | 1.2 [1.0 – 1.3] | 2.0 [1.7 – 2.1] | 1.1 [1.1 – 1.3] | 1.9 [1.8 – 2.0] |
| | MAM | 1.0 [0.9 – 1.2] | 1.7 [1.5 – 1.9] | 1.0 [0.9 – 1.3] | 1.5 [1.5 – 1.7] |
| | JJA | 1.2 [1.0 – 1.5] | 2.0 [1.7 – 2.3] | 1.3 [1.1 – 1.7] | 2.1 [1.7 – 2.5] |
| | SON | 1.2 [1.0 – 1.3] | 2.1 [1.9 – 2.2] | 1.3 [1.0 – 1.7] | 2.3 [1.9 – 2.8] |
| RCP8.5 (14) | ANN | 1.2 [1.0 – 1.4] | 3.6 [3.2 – 3.8] | 1.3 [0.9 – 1.5] | 3.8 [3.3 – 4.5] |
| | DJF | 1.2 [1.0 – 1.4] | 3.4 [3.0 – 3.8] | 1.2 [0.9 – 1.4] | 3.3 [2.9 – 3.8] |
| | MAM | 1.0 [0.9 – 1.1] | 3.0 [2.7 – 3.4] | 0.9 [0.7 – 1.2] | 2.9 [2.4 – 3.3] |
| | JJA | 1.4 [1.0 – 1.7] | 4.1 [3.4 – 4.7] | 1.4 [0.8 – 1.8] | 4.8 [3.9 – 5.6] |
| | SON | 1.4 [1.1 – 1.5] | 3.8 [3.3 – 4.1] | 1.5 [1.1 – 1.8] | 4.1 [3.4 – 4.4] |
| RCP8.5 (41) | ANN | 1.3 [1.1 – 1.6] | 3.7 [3.3 – 4.0] | 1.3 [1.1 – 1.5] | 3.9 [3.4 – 4.4] |
| | DJF | 1.4 [1.0 – 1.8] | 3.6 [3.0 – 4.1] | 1.3 [1.0 – 1.4] | 3.6 [3.1 – 4.0] |
| | MAM | 1.1 [0.9 – 1.3] | 3.2 [2.8 – 3.5] | 0.9 [0.9 – 1.0] | 3.0 [2.7 – 3.3] |
| | JJA | 1.4 [1.0 – 1.6] | 4.2 [3.7 – 4.6] | 1.3 [1.0 – 1.6] | 4.7 [4.3 – 5.2] |
| | SON | 1.5 [1.2 – 1.5] | 4.1 [3.4 – 4.1] | 1.5 [1.1 – 1.8] | 4.3 [3.5 – 4.6] |

Table S7. Average UHI over the historical period (1976–2005) for the 14 and 41 simulations ensemble. In addition to the mean, the spread of the ensemble is represented by the percentiles 25 and 75.

| | | $UHI_N$ | $UHI_X$ |
|---|---|---|---|
| | | 1976–2005 | 1976–2005 |
| Historical (14) | DJF | 2.40 [2.19 – 2.55] | 2.01 [1.78 – 2.05] |
| | MAM | 2.52 [2.29 – 2.67] | 1.33 [1.12 – 1.2] |
| | JJA | 2.06 [1.96 – 2.13] | 0.87 [0.80 – 0.94] |
| | SON | 2.32 [2.26 – 2.36] | 1.36 [1.15 – 1.25] |
| Historical (41) | DJF | 2.43 [2.14 – 2.63] | 2.02 [1.75 – 2.34] |
| | MAM | 2.62 [2.36 – 2.79] | 1.34 [1.15 – 1.44] |
| | JJA | 2.17 [2.00 – 2.30] | 0.78 [0.63 – 0.90] |
| | SON | 2.49 [2.28 – 2.71] | 1.32 [1.14 – 1.32] |

Table S8. Same as table S4 but for the 90$^{th}$ percentile of UHI instead of the average UHI.

| | | $P_{90}UHI_N$ | $P_{90}UHI_X$ |
|---|---|---|---|
| | | 1976–2005 | 1976–2005 |
| Historical (14) | DJF | 3.57 [3.34 – 3.84] | 3.21 [2.85 – 3.32] |
| | MAM | 3.86 [3.64 – 4.1] | 1.97 [1.63 – 2.03] |
| | JJA | 3.02 [2.86 – 3.11] | 1.47 [1.38 – 1.46] |
| | SON | 3.41 [3.29 – 3.42] | 2.27 [1.92 – 2.18] |
| Historical (41) | DJF | 3.69 [3.25 – 4.03] | 3.17 [2.72 – 3.69] |
| | MAM | 4.11 [3.78 – 4.58] | 2.01 [1.67 – 2.18] |
| | JJA | 3.23 [2.96 – 3.5] | 1.41 [1.31 – 1.45] |
| | SON | 3.72 [3.37 – 4.15] | 2.25 [1.94 – 2.42] |

Table S9. Projected average UHI change in the near and far future (2030–2049 and 2080–2099) in comparison to the historical period (1976–2005). In addition to the mean, the spread of the ensemble is represented by the percentiles 25 and 75.

| | | $\Delta UHI_N$ | | $\Delta UHI_X$ | |
|---|---|---|---|---|---|
| | | 2030–2049 | 2080–2099 | 2030–2049 | 2080–2099 |
| RCP4.5 (14) | DJF | -0.02 [-0.05 – 0.01] | -0.03 [-0.06 – 0.01] | -0.08 [-0.11 – -0.04] | -0.12 [-0.13 – -0.10] |
| | MAM | -0.02 [-0.07 – 0.03] | -0.04 [-0.09 – 0.00] | 0.00 [-0.01 – 0.01] | 0.00 [-0.01 – 0.01] |
| | JJA | -0.06 [-0.11 – -0.01] | -0.07 [-0.11 – -0.04] | -0.05 [-0.08 – -0.02] | -0.07 [-0.12 – -0.05] |
| | SON | -0.03 [-0.05 – 0.00] | -0.08 [-0.12 – -0.05] | -0.04 [-0.06 – -0.02] | -0.06 [-0.09 – -0.02] |
| RCP8.5 (14) | DJF | -0.03 [-0.06 – 0.01] | -0.03 [-0.07 – 0.05] | -0.10 [-0.15 – -0.06] | -0.13 [-0.2 – -0.10] |
| | MAM | -0.02 [-0.07 – 0.02] | -0.11 [-0.23 – 0.00] | -0.01 [-0.02 – 0.00] | 0.00 [-0.03 – 0.02] |
| | JJA | -0.05 [-0.08 – -0.04] | -0.19 [-0.24 – -0.14] | -0.03 [-0.08 – 0.00] | -0.16 [-0.22 – -0.09] |
| | SON | -0.05 [-0.09 – -0.01] | -0.14 [-0.21 – -0.07] | -0.04 [-0.07 – -0.02] | -0.10 [-0.12 – -0.08] |
| RCP8.5 (41) | DJF | 0.00 [-0.05 – 0.05] | 0.02 [-0.04 – 0.07] | -0.08 [-0.12 – -0.02] | -0.13 [-0.22 – -0.07] |
| | MAM | -0.02 [-0.07 – 0.02] | -0.10 [-0.17 – -0.03] | 0.00 [-0.01 – 0.02] | 0.02 [-0.02 – 0.06] |
| | JJA | -0.07 [-0.11 – -0.04] | -0.22 [-0.29 – -0.13] | -0.04 [-0.09 – 0.00] | -0.16 [-0.23 – -0.07] |
| | SON | -0.05 [-0.09 – -0.01] | -0.14 [-0.19 – -0.06] | -0.05 [-0.07 – -0.02] | -0.10 [-0.13 – -0.08] |

Table S10. Projected average UHI in the near and far future (2030–2049 and 2080–2099) in comparison to the historical period (1976–2005). In addition to the mean, the spread of the ensemble is represented by the percentiles 25 and 75.

| | | $UHI_N$ | | $UHI_X$ | |
|---|---|---|---|---|---|
| | | 2030–2049 | 2080–2099 | 2030–2049 | 2080–2099 |
| RCP4.5 (14) | DJF | 2.38 [2.21 – 2.52] | 2.37 [2.19 – 2.49] | 1.94 [1.69 – 1.94] | 1.89 [1.68 – 1.85] |
| | MAM | 2.50 [2.31 – 2.60] | 2.48 [2.31 – 2.55] | 1.33 [1.13 – 1.18] | 1.33 [1.11 – 1.20] |
| | JJA | 2.01 [1.92 – 2.03] | 1.99 [1.90 – 2.03] | 0.83 [0.75 – 0.88] | 0.80 [0.70 – 0.89] |
| | SON | 2.29 [2.21 – 2.31] | 2.24 [2.17 – 2.25] | 1.33 [1.13 – 1.25] | 1.30 [1.10 – 1.24] |
| RCP8.5 (14) | DJF | 2.37 [2.18 – 2.51] | 2.37 [2.27 – 2.48] | 1.91 [1.69 – 1.94] | 1.88 [1.63 – 1.85] |
| | MAM | 2.49 [2.32 – 2.59] | 2.41 [2.27 – 2.46] | 1.32 [1.10 – 1.21] | 1.33 [1.10 – 1.22] |
| | JJA | 2.01 [1.91 – 2.03] | 1.88 [1.74 – 1.95] | 0.84 [0.77 – 0.92] | 0.71 [0.60 – 0.81] |
| | SON | 2.27 [2.20 – 2.30] | 2.18 [2.11 – 2.19] | 1.32 [1.10 – 1.23] | 1.26 [1.04 – 1.23] |
| RCP8.5 (41) | DJF | 2.44 [2.21 – 2.66] | 2.45 [2.25 – 2.62] | 1.94 [1.68 – 2.18] | 1.89 [1.64 – 2.08] |
| | MAM | 2.60 [2.37 – 2.75] | 2.52 [2.28 – 2.70] | 1.34 [1.15 – 1.44] | 1.35 [1.18 – 1.39] |
| | JJA | 2.09 [1.96 – 2.19] | 1.95 [1.84 – 2.02] | 0.74 [0.59 – 0.85] | 0.63 [0.46 – 0.75] |
| | SON | 2.44 [2.22 – 2.70] | 2.36 [2.13 – 2.60] | 1.27 [1.08 – 1.29] | 1.22 [1.03 – 1.23] |

Table S11. Projected 90th percentile UHI change in the near and far future (2030–2049 and 2080–2099) in comparison to the historical period (1976–2005). In addition to the mean, the spread of the ensemble is represented by the percentiles 25 and 75.

| | | $UHI_N$ | | $UHI_X$ | |
|---|---|---|---|---|---|
| | | 2030–2049 | 2080–2099 | 2030–2049 | 2080–2099 |
| RCP4.5 (14) | DJF | -0.05 [-0.12 – -0.01] | -0.07 [-0.17 – 0.00] | -0.23 [-0.33 – -0.12] | -0.31 [-0.34 – -0.23] |
| | MAM | -0.04 [-0.11 – 0.04] | -0.09 [-0.15 – -0.03] | 0 [-0.02 – 0.03] | 0.01 [-0.03 – 0.06] |
| | JJA | -0.08 [-0.12 – -0.03] | -0.09 [-0.14 – -0.06] | -0.02 [-0.04 – 0] | -0.04 [-0.05 – 0.01] |
| | SON | -0.08 [-0.13 – -0.02] | -0.15 [-0.21 – -0.09] | -0.02 [-0.06 – 0.01] | -0.04 [-0.09 – 0.00] |
| RCP8.5 (14) | DJF | -0.06 [-0.13 – 0.02] | -0.04 [-0.16 – 0.13] | -0.29 [-0.37 – -0.16] | -0.39 [-0.47 – -0.32] |
| | MAM | -0.04 [-0.12 – 0.05] | -0.23 [-0.42 – -0.05] | 0.01 [-0.01 – 0.02] | -0.01 [-0.07 – 0.02] |
| | JJA | -0.07 [-0.12 – -0.04] | -0.24 [-0.31 – -0.21] | -0.01 [-0.04 – 0.02] | -0.08 [-0.10 – -0.02] |
| | SON | -0.08 [-0.15 – -0.03] | -0.21 [-0.32 – -0.11] | -0.04 [-0.07 – 0] | -0.07 [-0.11 – -0.04] |
| RCP8.5 (41) | DJF | 0.02 [-0.06 – 0.12] | 0.05 [-0.05 – 0.14] | -0.21 [-0.32 – -0.08] | -0.36 [-0.48 – -0.22] |
| | MAM | -0.03 [-0.13 – 0.06] | -0.21 [-0.38 – -0.04] | 0.01 [-0.01 – 0.04] | 0.02 [-0.07 – 0.09] |
| | JJA | -0.1 [-0.15 – -0.05] | -0.33 [-0.42 – -0.22] | -0.02 [-0.05 – 0.01] | -0.08 [-0.15 – -0.02] |
| | SON | -0.09 [-0.15 – -0.04] | -0.22 [-0.33 – -0.13] | -0.04 [-0.08 – 0] | -0.09 [-0.12 – -0.04] |

Table S12. Projected 90th percentile UHI in the near and far future (2030–2049 and 2080–2099) in comparison to the historical period (1976–2005). In addition to the mean, the spread of the ensemble is represented by the percentiles 25 and 75.

| | | $UHI_N$ | | $UHI_X$ | |
|---|---|---|---|---|---|
| | | 2030–2049 | 2080–2099 | 2030–2049 | 2080–2099 |
| RCP4.5 (14) | DJF | 3.52 [3.4 – 3.76] | 3.49 [3.29 – 3.79] | 2.98 [2.67 – 2.96] | 2.9 [2.55 – 2.83] |
| | MAM | 3.82 [3.62 – 4.01] | 3.77 [3.58 – 3.87] | 1.98 [1.63 – 2] | 1.99 [1.62 – 2.03] |
| | JJA | 2.94 [2.78 – 2.99] | 2.92 [2.75 – 2.97] | 1.45 [1.35 – 1.44] | 1.43 [1.33 – 1.44] |
| | SON | 3.33 [3.17 – 3.37] | 3.26 [3.09 – 3.36] | 2.25 [1.91 – 2.1] | 2.23 [1.91 – 2.12] |
| RCP8.5 (14) | DJF | 3.51 [3.36 – 3.78] | 3.53 [3.47 – 3.72] | 2.92 [2.58 – 3.01] | 2.82 [2.46 – 2.76] |
| | MAM | 3.83 [3.66 – 3.94] | 3.63 [3.42 – 3.66] | 1.98 [1.6 – 2.06] | 1.96 [1.55 – 2] |
| | JJA | 2.95 [2.79 – 2.99] | 2.78 [2.59 – 2.85] | 1.46 [1.36 – 1.5] | 1.39 [1.29 – 1.47] |
| | SON | 3.32 [3.16 – 3.41] | 3.2 [3.07 – 3.28] | 2.23 [1.87 – 2.08] | 2.2 [1.87 – 2.08] |
| RCP8.5 (41) | DJF | 3.71 [3.37 – 4.11] | 3.74 [3.46 – 4.13] | 2.96 [2.58 – 3.46] | 2.81 [2.43 – 3.07] |
| | MAM | 4.08 [3.7 – 4.53] | 3.9 [3.49 – 4.33] | 2.03 [1.68 – 2.16] | 2.03 [1.74 – 2.14] |
| | JJA | 3.13 [2.93 – 3.38] | 2.9 [2.71 – 3.13] | 1.39 [1.27 – 1.46] | 1.33 [1.21 – 1.41] |
| | SON | 3.63 [3.28 – 4.07] | 3.49 [3.08 – 3.87] | 2.21 [1.89 – 2.28] | 2.17 [1.87 – 2.26] |

Table S13. Projected maximum $TN_{URB}$ and $TX_{URB}$ in the near and far future (2030–2049 and 2080–2099) in comparison to the historical period (1976–2005). In addition to the mean, the spread of the ensemble is represented by the percentiles 25 and 75.

| | | $TN_{URB}$ | | $TX_{URB}$ | |
|---|---|---|---|---|---|
| | | 2030–2049 | 2080–2099 | 2030–2049 | 2080–2099 |
| RCP4.5 (14) | DJF | 15.7 [14.8 – 16.1] | 16.6 [15.6 – 17.8] | 21.4 [19.7 – 22.5] | 22.8 [21.6 – 23.5] |
| | MAM | 22.5 [22.1 – 23] | 22.2 [21.3 – 23.5] | 33.7 [32.2 – 34.5] | 33.1 [31.6 – 34] |
| | JJA | 26.1 [24.9 – 26.6] | 27.4 [25.8 – 28.4] | 39.8 [38.6 – 41.6] | 40.2 [37.7 – 41.9] |
| | SON | 22.4 [21.7 – 22.6] | 23.5 [23.1 – 24.3] | 35 [33.2 – 37.2] | 35.6 [32.7 – 38.5] |
| RCP8.5 (14) | DJF | 15.7 [14.9 – 16.1] | 17.8 [16.8 – 18.6] | 21.7 [20.3 – 23] | 23.5 [21.5 – 25.9] |
| | MAM | 21.2 [19.9 – 21.8] | 24.5 [23.5 – 24.7] | 32.7 [31.3 – 33.4] | 35.2 [34.4 – 36] |
| | JJA | 26.4 [25.3 – 27.4] | 30.2 [29.1 – 31.1] | 39.1 [37.5 – 40.4] | 43.9 [40.8 – 46.5] |
| | SON | 23.2 [22.6 – 23.9] | 25.9 [24.3 – 26.9] | 33.9 [32.5 – 36.2] | 38.5 [35.8 – 40.8] |
| RCP8.5 (41) | DJF | 15.3 [14.4 – 15.9] | 17.7 [16.5 – 18.2] | 21.2 [19.2 – 22.6] | 23.2 [21.3 – 24.4] |
| | MAM | 21.9 [20.7 – 23] | 24.9 [24 – 25.7] | 33.1 [31.6 – 34.1] | 36.2 [34.2 – 38.1] |
| | JJA | 27.5 [25.8 – 28.8] | 30.9 [29.5 – 32] | 39.4 [37.1 – 41.7] | 43.7 [40.7 – 46.6] |
| | SON | 23.5 [22.5 – 24.2] | 26.4 [25 – 27.8] | 33.9 [32.2 – 36.1] | 38.3 [35.8 – 41.4] |

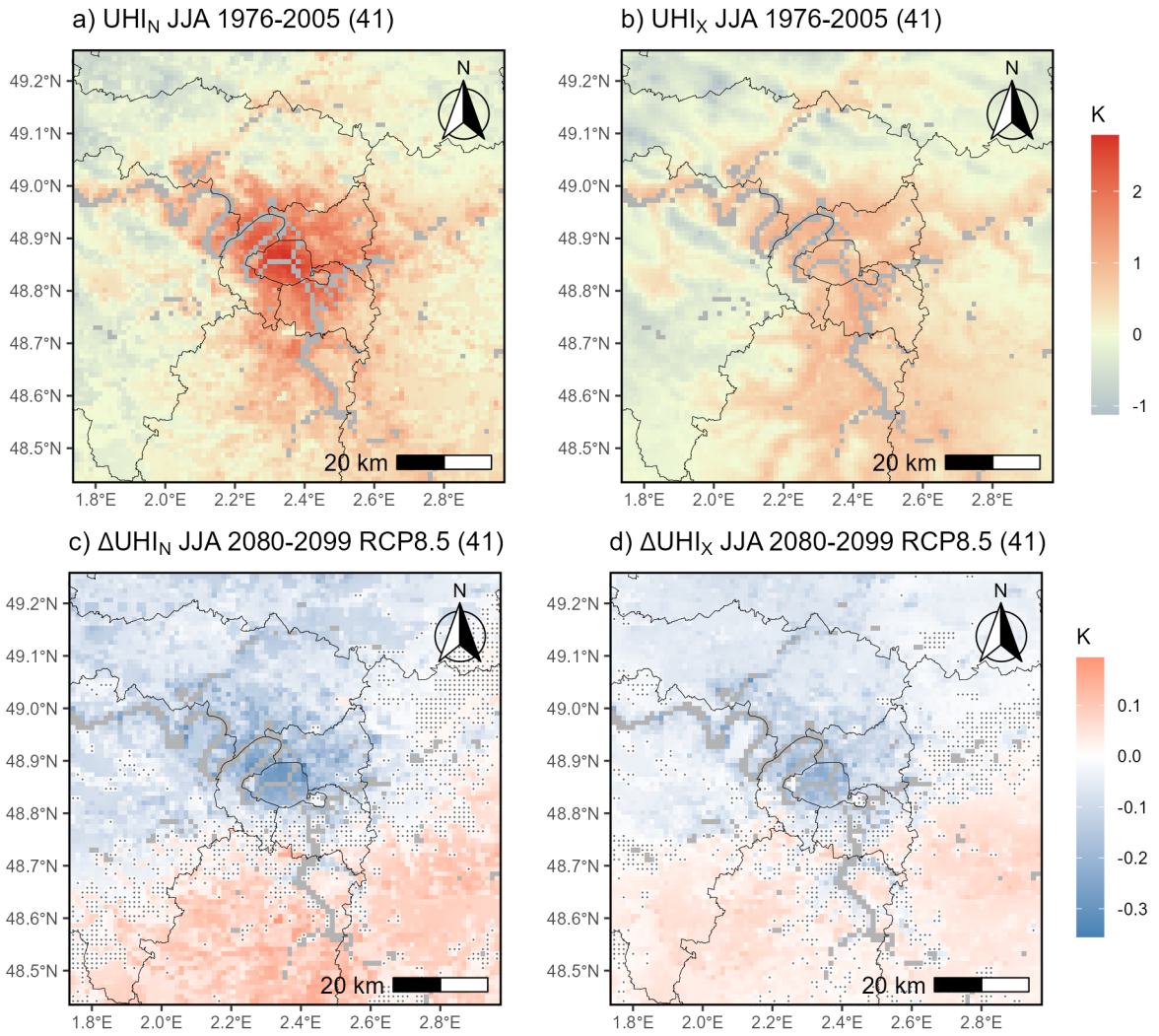


Fig. S2. Average seasonal $UHI_N$ and $UHI_X$ maps for JJA over the historical period 1976–2005 and differences in 2080–2099 for scenario RCP8.5 and the 41 simulations. Daily UHIs maps are obtained by subtracting $TN_{RUR}$/$TX_{RUR}$ from the temperature field. The gray areas represent points with more than 5% water body coverage that are removed. The gray dots represent points where less than 66% of the models (27/41) agree on the sign of the change.

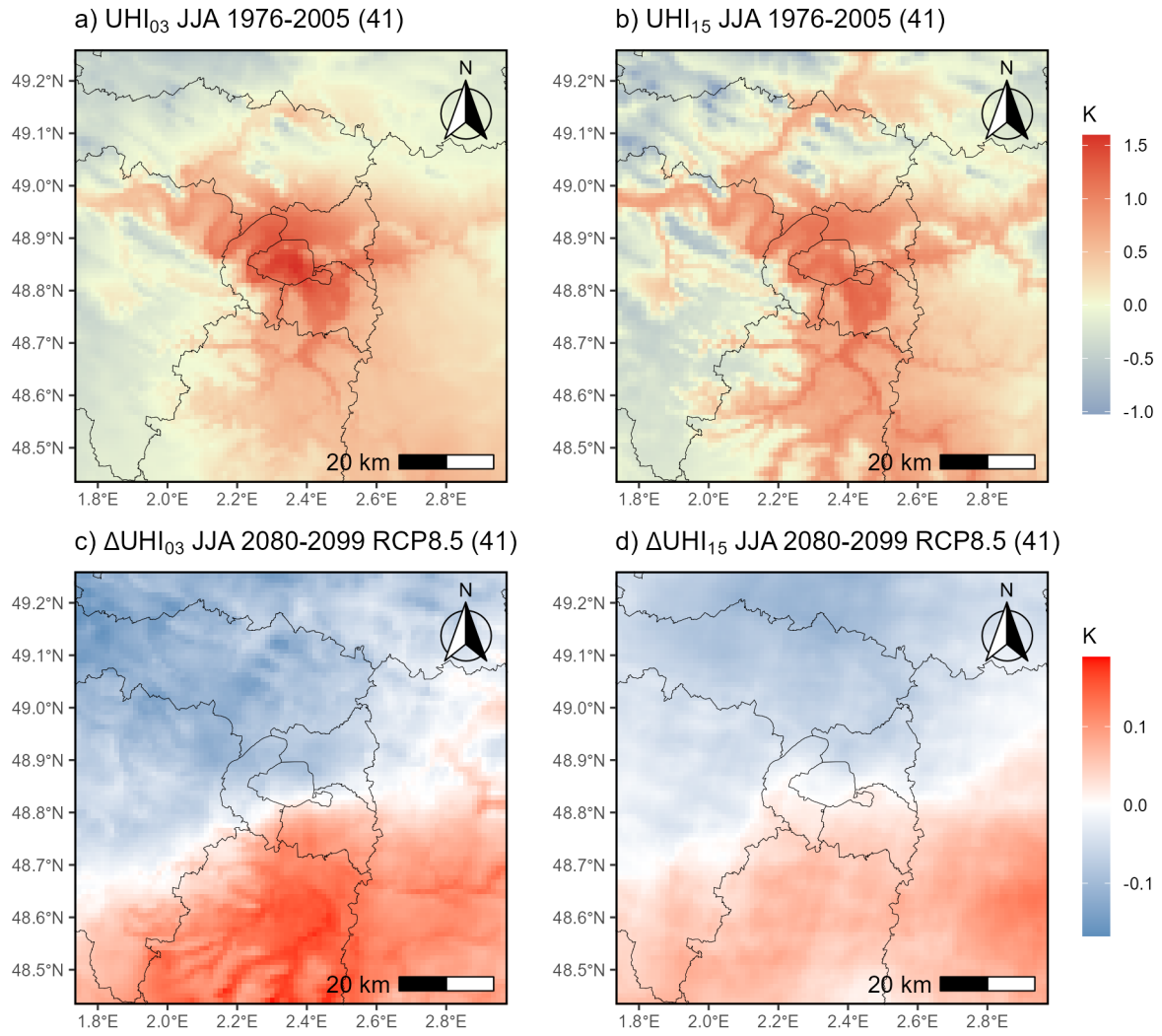


Fig. S3. Average seasonal forcing UHI maps (50 m) at 03 UTC and 15 UTC for JJA over the historical period 1976–2005 and differences in 2080–2099 for scenario RCP8.5 for the 41 simulations.

SUPPLEMENTAL MATERIAL REFERENCES

Bentsen, M., Bethke, I., Debernard, J. B., Iversen, T., Kirkevåg, A., Seland, Ø., ... & Kristjansson, J. E. (2013). The Norwegian Earth System Model, NorESM1–M–Part 1: description and basic evaluation of the physical climate. Geoscientific Model Development, 6(3), 687–720.

Christensen, O. B., Drews, M., Christensen, J. H., Dethloff, K., Ketelsen, K., Hebestadt, I., & Rinke, A. (2007). The HIRHAM regional climate model. Version 5 (beta).

Collins, W. J., Bellouin, N., Doutriaux–Boucher, M., Gedney, N., Halloran, P., Hinton, T., ... & Woodward, S. (2011). Development and evaluation of an Earth–System model–HadGEM2. Geoscientific Model Development, 4(4), 1051–1075.

Daniel, M., Lemonsu, A., Déqué, M., Somot, S., Alias, A., & Masson, V. (2019). Benefits of explicit urban parameterization in regional climate modeling to study climate and city interactions. Climate Dynamics, 52(5–6), 2745–2764.

Dufresne, J. L., Foujols, M. A., Denvil, S., Caubel, A., Marti, O., Aumont, O., ... & Vuichard, N. (2013). Climate change projections using the IPSL–CM5 Earth System Model: from CMIP3 to CMIP5. Climate dynamics, 40(9), 2123–2165.

Erbs, D. G., Klein, S. A., & Duffie, J. A. (1982). Estimation of the diffuse radiation fraction for hourly, daily and monthly–average global radiation. *Solar energy*, *28*(4), 293–302.

Giorgetta, Marco A., et al. "Climate and carbon cycle changes from 1850 to 2100 in MPI-ESM simulations for the Coupled Model Intercomparison Project phase 5." Journal of Advances in Modeling Earth Systems 5.3 (2013): 572–597.

Giorgi, F., Coppola, E., Solmon, F., Mariotti, L., Sylla, M. B., Bi, X., ... & Brankovic, C. (2012). RegCM4: model description and preliminary tests over multiple CORDEX domains. Climate Research, 52, 7–29.

Hazeleger, W., Severijns, C., Semmler, T., Ştefănescu, S., Yang, S., Wang, X., ... & Willén, U. (2010). EC–Earth: a seamless earth–system prediction approach in action. Bulletin of the American Meteorological Society, 91(10), 1357–1364.

Hazeleger, W., Wang, X., Severijns, C., Ştefănescu, S., Bintanja, R., Sterl, A., ... & Van der Wiel, K. (2012). EC–Earth V2. 2: description and validation of a new seamless earth system prediction model. Climate dynamics, 39(11), 2611–2629.

Iversen, T., Bentsen, M., Bethke, I., Debernard, J. B., Kirkevåg, A., Seland, Ø., ... & Seierstad, I. A. (2013). The Norwegian earth system model, NorESM1–M–Part 2: climate response and scenario projections. Geoscientific Model Development, 6(2), 389–415.

Jacob, D., Elizalde, A., Haensler, A., Hagemann, S., Kumar, P., Podzun, R., ... & Wilhelm, C. (2012). Assessing the transferability of the regional climate model REMO to different coordinated regional climate downscaling experiment (CORDEX) regions. Atmosphere, 3(1), 181–199.

Jennings, K. S., Winchell, T. S., Livneh, B., & Molotch, N. P. (2018). Spatial variation of the rain–snow temperature threshold across the Northern Hemisphere. *Nature communications*, *9*(1), 1148.

Le Roy, B. (2021b). *Méthodologie d'étude des impacts du changement climatique sur la ville par descente d'échelle statistico–dynamique: application à la région parisienne* (Doctoral dissertation, Université Paul Sabatier–Toulouse III).

Le Roy, B., Lemonsu, A., & Schoetter, R. (2021a). A statistical–dynamical downscaling methodology for the urban heat island applied to the EURO–CORDEX ensemble. *Climate Dynamics*, *56*, 2487–2508.

Lemonsu, A., Kounkou–Arnaud, R., Desplat, J., Salagnac, J. L., & Masson, V. (2013). Evolution of the Parisian urban climate under a global changing climate. Climatic change, 116(3), 679–692.

Mezghani, A., Dobler, A., Benestad, R., Haugen, J. E., Parding, K. M., Piniewski, M., & Kundzewicz, Z. W. (2019). Subsampling impact on the climate change signal over Poland based on simulations from statistical and dynamical downscaling. *Journal of Applied Meteorology and Climatology*, *58*(5), 1061–1078.

Samuelsson, P., Gollvik, S., Kupiainen, M., Kourzeneva, E., & van de Berg, W. J. (2015). The surface processes of the Rossby Centre regional atmospheric climate model (RCA4). SMHI.

Sørland, S. L., Brogli, R., Pothapakula, P. K., Russo, E., Van de Walle, J., Ahrens, B., ... & Thiery, W. (2021). COSMO–CLM regional climate simulations in the Coordinated Regional Climate Downscaling Experiment (CORDEX) framework: a review. Geoscientific Model Development, 14(8), 5125–5154.

Tornay, N., Schoetter, R., Bonhomme, M., Faraut, S., & Masson, V. (2017). GENIUS: A methodology to define a detailed description of buildings for urban climate and building energy consumption simulations. *Urban Climate*, *20*, 75–93.

van Meijgaard, E., Van Ulft, L. H., Lenderink, G., De Roode, S. R., Wipfler, E. L., Boers, R., & van Timmermans, R. M. A. (2012). Refinement and application of a regional atmospheric model for climate scenario calculations of Western Europe (No. KVR 054/12). KVR.

van Meijgaard, E., Van Ulft, L. H., Van de Berg, W. J., Bosveld, F. C., Van den Hurk, B. J. J. M., Lenderink, G., & Siebesma, A. P. (2008). The KNMI regional atmospheric climate model RACMO, version 2.1 (p. 43). De Bilt, The Netherlands: KNMI.

Voldoire, A., Sanchez–Gomez, E., Salas y Mélia, D., Decharme, B., Cassou, C., Sénési, S., ... & Chauvin, F. (2013). The CNRM–CM5. 1 global climate model: description and basic evaluation. Climate dynamics, 40(9), 2091–2121.